Hybrid Perovskites for a Renewable Revolution

A Dissertation presented to
La Escuela Técnica Superior de Ingeniería del Diseño
Universitat Politècnica de València

By Alexander W. Stewart

Supervised by Prof. Dr. Bernabé Marí Soucase and Dr. Erika Vega

In Partial Fulfilment of the Requirements for the Master in Sensors for Industrial Applications

Valencia, 11th September 2019

Hybrid Perovskites for a Renewable Revolution

Abstract

Hybrid organic-inorganic perovskites have emerged, within a wider set of applications, as a leading candidate for solar power generation. Focusing on methylamonium lead-based perovskites, halide content is varied, demonstrating the tune-ability of the band-gap energy. These band-gap energies are shown to range over the visible spectrum, facilitating their use in photovoltaic applications. Building upon these results, perovskite layers are inserted into fully functioning devices. Producing promising results, this project is to lay the foundations for further investigations into perovskites and compositional engineering.

Resumen

Las perovskitas híbridas organicas-inorgánicas han surgido como una alternativa viable y eficiente para la generación de energía solar, además de para muchas otras aplicaciones. A partir de las perovskitas de metilamonio y plomo, se ha probado la capacidad de ajuste de la energía del band-gap a lo largo del espectro visible en función de la cantidad de haluro empleado en la composición, lo que facilita su empleo en aplicaciones fotovoltaicas. A partir de los resultados obtenidos se han sintetizado diferentes capas de perovskitas para su empleo en dispositivos fotovoltaicos. Los resultados obtenidos han sido muy prometedores y establecen las bases para futuras investigaciones en materiales de perovskita e ingeniería composicional.

Key Words: Perovskites, Solar Power, Renewable Energy, Photovoltaic, Band-Gap Tune-ability, Compositional Engineering

Palabras claves: perovskitas, energía solar, energía renovable, fotovoltaica, banda prohibida, ingeniería de composición

Alumno: Alexander W. Stewart

Tutores Académicos: Prof. Dr. Bernabé Marí Soucase y Dr. Erika Vega

Valencia, 11 Septiembre 2019

Contents

1 Introduction

1.1 Objectives

Following the immediate threat posed to humanity by climate change, the accelerated move to renewable power sources has been identified as key to our survival (Paris Agreement).

Within the renewable energy sector, solar panels have attracted attention due to the reliability and predictability of their power generation when compared with other sources such as wind or tidal. Solar based technologies are also built upon far richer physics; having no moving parts, their power generation is best understood in the language of Quantum Mechanics and Condensed Matter Physics. For these reasons, the aim of this Masters dissertation is to aid this shift to a clean and sustainable future by investigating and developing super cheap and ultra-efficient solar power based on perovskite materials.

In order to bring solar cells (SCs) to the market, the challenge is to reduce the price per unit energy produced in order to bring them into competition with established fossil fuel sources. To achieve this, one can either increase the efficiency of the cells or decrease the price of their production. Perovskite based SCs are known to be one of the fastest growing solar technologies in terms of efficiency (see Figure 1) and also benefit from low production costs when compared with their silicon counterparts. Cost analysis suggests that a module efficiency higher than 12% with stability longer than 12 years and an aperture area of 1 m^2 are necessary conditions to achieve electricity generation costs below traditional sources, which is around 6 US cents kWh^{-1} [1].

On one hand, the large gains made in the efficiencies of perovskites SCs is driven by their impressive optoelectronic properties, which has even led some to predict that organic cells will break the Shockley-Queisser limit [2]. On the other hand, the widespread interest in perovskites stimulated by the initial investigations into their fabrication has led to extensive research into many of their aspects over a short period of time. For example, unlike their silicon counterparts which require clean rooms, vacuums and other expensive high-tech equipment, perovskite SCs can be manufactured with relative ease. Perovskite SCs can be synthesised via solution deposition methods, leading to lower costs [3] and an opportunity to automate production [4, 5].

However, a current difficulty with perovskites is that they suffer from stability problems which greatly influence their predicted lifespan [6]. Organic parts of perovskite SCs tend to react with humidity, degrading back into their precursor elements. For all their promise, perovskite cells will not be take the market by storm until they can be stabilized for long-term use.

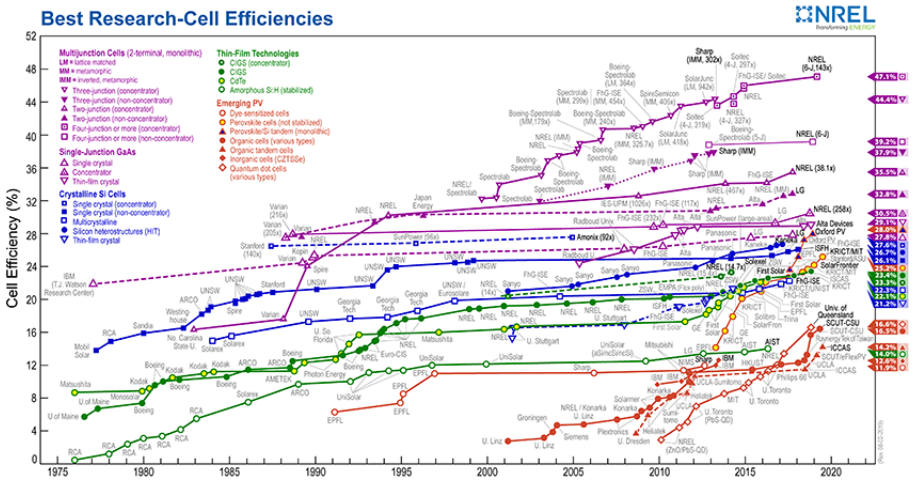

Figure 1: Shows the highest efficiencies achieved within a research environment [7]. Perovskite cells are represented as yellow-filled orange circles. The rate of increase in efficiency can be seen to be substantially higher than for other SCs.

1.2 Solar Cells

1.2.1 Background

SCs are broadly categorised into three generations. First generation cells comprise of crystalline silicon and still dominate the market. They benefit from high efficiencies, up to 27.6% (Figure 1), and long term life-spans often spanning decades. Moreover, many of these silicon-based devices have benefited from rapid falls in price [8]. On the other hand, these cells require energetically intensive manufacturing processes in order to yield high-grade silicon. This not only inflates the price of the cells on the market but also offsets their benefits in the context of the necessary shift to renewable and sustainable power sources.

Second generation SCs have inorganic light absorbing layers with high extinction coefficients. Since these SCs are based on thin films, around 1 µm thick, they are commonly known as thin film SCs. Cadium telluride (CdTe) has the second largest market share after silicon based technologies, due to the structural simplicity [9] and the high efficiencies achieved, of up to 22.7% [10].

The third, and latest, generation of SCs encompass a wide range of technologies, including quantum dots [11], dye-sensitive SCs (DSSC) [12], multi-junction SCs and organic SCs. The latter being the focus of this dissertation. Organic materials benefit from low-cost production methods [13] and can have great con-

ductive and radiative properties. The main limitation of organic materials is their inherent short term instability, in contrast to certain inorganic materials. Hence, the search is on, for an organic-inorganic material with all the desired properties. These synthetic materials are generically called organic-inorganic hybrid (OIH) materials.

1.2.2 Organic-Inorganic Hybrid Perovskites

OIH materials have opened up new possibilities within the context of photovoltaics. They grant the ability to use organic absorbers in combination with the dielectric screening of inorganic components. This allows for easier dissociation between free charge carriers and an increased efficiency in the transportation to their corresponding electrode. Compositional engineering, by varying quantities of each organic/inorganic ingredient, empowers researchers to yield very different: interface structures, excitation lifetimes, charge-carrier transport properties and optoelectronic properties.

One of the most fascinating types of OIH SCs are known as Perovskites. Their SC efficiencies have gone from 3.8%[14] in 2009, up to 25.2% in a mere ten years (Figure 1). They are made from low-cost materials and can be fabricated in low temperature environments. Moreover they have competitive efficiencies when compared against multi-crystalline silicon SCs (see Figure 1). This high efficiency is ultimately driven by the low band-gap of the methylammonium lead iodide and a low loss-in potential. In the future, further reductions in the loss-in potential are expected to take place, originating from lowering the density of trap states which catalyse recombinations.

In powder form it has a white appearance, however when it crystallizes it turns dark, with a tint of orange and brown. Apart from its dark colour (meaning it absorbs a large range of radiation energies), another reason it is so popular for use in SCs is that it has a band-gap energy that falls within the visible spectrum. Moreover this gap can be finely tuned through substitution of the halide [15], cations or anions.

A perovskite SC is a PN junction, formed from an n-type and a p-type material. Through electron-hole creation in the perovskite layer, ions can be collected by sandwiching it between a cathode and an anode, allowing the powering of an external load.

The anode, used to conduct electrons, is made up of a conductive glass layer coated with a conductive layer, such as transparent fluorine doped tin oxide (FTO). On top of this, a layer of n-type titanium dioxide TiO_2 semiconductor is usually deposited. A perovskite layer, commonly methylammonium lead halide, is then deposited on top to serve as a source of electrons and holes. Upon this, a thin

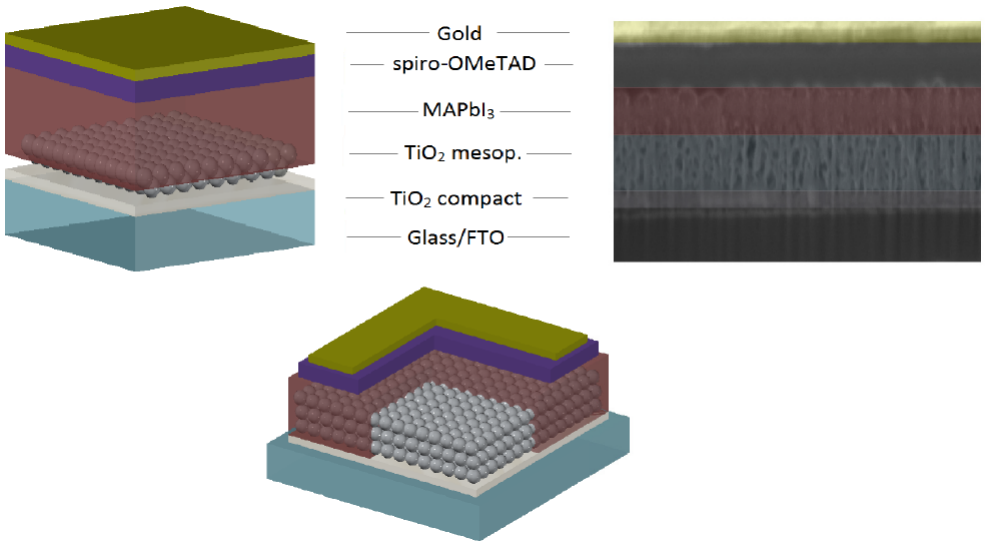

Figure 2: Cross-sectional image of an FESEM image for a mesoporous oxide based perovskite SC [16].

layer of spiro-OMeTAD, back contacted with gold, is deposited to transport holes. Hence this layer can be thought of as the cathode.

The heart of the SC is the perovskite absorber, which is a semiconductor. In the case of incident photons having energies lower than the band-gap $h\nu < E_g$, then it becomes highly probable that the photon will be transmitted through the material in question. Independent of the band-gap structure, there also exists the possibility of the photon being reflected off the surface of a material. This physical property of a material is characterised by the reflectivity of a sample, which is known to be dependent on the properties of the surface such as roughness and colour. Therefore information about the suitability of a perovskite for solar applications can be deduced from both crystal and film morphology at the nano-scale as well as macroscopic properties and defects.

1.3 Wider Applications of Perovskites

Following the discovery of the perovskite mineral $CaTiO_3$ by Gustav Rose, in 1839, the family of materials with the chemical formula ABX_3, known as perovskites, was established. Perovskites are now known to have several important properties, ranging from ones with useful technological applications such as piezoelectricity,

high thermopower, magnetism and super and semi conductivity to more specialized applications using perovskite's colossal magnetoresistivity, charge ordering and spin dependent transport [17].

Around a century after Rose's discovery, Physicist Percy Williams Bridgman demonstrated that the most abundant mineral on the planet was a perovskite which forms under the high pressures found in the lower mantel, accounting for 93% of the lower mantle and 38% of the minerals on the planet [18]. For his discovery of (Mg, Fe)SiO_3, more commonly known as Bridgmanite, Bridgman received the Nobel Prized in 1946.

Some years later, J. Georg Bednorz and K. Alexander Müller discovered the ceramic "High temperature superconductors" based on the perovskite-like structures of La_2CuO_4 and $YBa_2Cu_3O_6$. They found that these perovskites can be insulating or super-conductive at temperatures up to 138K, depending on oxygen content. As such, this is the first example of compositionally engineering perovskites. For their work, in 1987 they would be awarded the Nobel Prize.

Since then, major avenues of research have been established following the discovery of perovskite's semi-conducting properties and, in turn, their widely ranging applications. Their stability issues aside, perovskites offer a potential alternative to many silicon based technologies since they benefit from brilliant optoelectronic properties and low manufacturing costs. This means that not only do perovskites find applications in SCs but radiative recombinations taking place within them also enable their use in LEDs [19, 20] and quantum dots. It has been shown that when $LaAlO_3$ is doped with neodymium it gives a laser emission at 1080nm [21].

In terms of lesser known applications, perovskites have been implemented in memory devices [22] and spintronics [23]. Perovskites are increasingly exploited in the microelectronics and telecommunications industries. In 2014 a research group at EPFL, Lausanne Switzerland, claimed that water electrolysis had been achieved with an efficiency of 12.3% [24] using perovskites. If correct, this breakthrough would facilitate the simple and cheap extraction of hydrogen from water, driving the use of hydrogen fuel cells and the move towards sustainable energy sources.

1.4 Outlook

This dissertation aims to achieve a number of goals, starting with a review of the literature on methylamonium lead perovskites.

The main body of the work investigates engineering the compositional, and structural, properties of the perovskites absorber, focusing on the tune-ability of the band structure by changing the relative halide concentration. Perovskite lay-

ers are synthesized, characterised and analysed using photo-luminescence, transmittance and X-ray diffraction tests, where results are presented within the context of perovskite stability.

Finally, perovskite layers are inserted into SC devices. The development and reproduction of these methods is intended to lay the ground work for the next stages of investigations into perovskite based SCs.

2 Literature Review

2.1 Methylamonium Lead Halides

Following a great deal of investigation over the past decade, the $MAPbI_3$ (MAPI) perovskite is arguably the most well understood within the context of photovoltaic applications. However many aspects still remain hotly debated, such as the source of the current-voltage hysteresis [25]. This review will examine several of their well understood properties, which make them favourable, or not, for their use in SCs, focusing on photo-ionisation driven excitations and their properties, degradation mechanisms and compositional engineering.

2.1.1 The Nature of Excitations

In the literature, the high efficiencies of MAPI perovskites are often attributed to their low exciton binding energy, relative to the thermal energy at ambient temperature [26, 27]. These authors suggest that this allows for easier charge separation and a situation when most carriers are present as free holes or free electrons [28, 29]. To gain a further insight into these claims, let us first examine the excitations taking place within these materials.

Excitations caused by photo-ionization in semiconductors are understood in terms of the creation of electron-hole pairs. Depending on the nature of of the ionising source, these electron-hole pairs may separate into free charge carriers or they may become a bound state, known as an exciton. In Quantum Mechanics, bound states are characterised by the localisation of a particle or quasi-particle due to the application of a potential. In the case of semiconductors, electron-hole pairs may become localised due to Coulombic forces or distortions in the lattice. The latter are known as self-bounded excitons, which take place when an exciton is shielded by phonons in such a way that the lattice deforms into a local potential, trapping the exciton.

The nature of these excitons has important implications for the application of semiconductors, such as perovskites. This is because although excitons have the ability to transport energy they are electrically neutral, meaning that they do not contribute to the electricity generated by SCs. On the other hand, excitons are known to degrade via radiative recombination and therefore have no impact on the quantum efficiencies of devices such as LEDs. Due to the trapped nature of excitons, they have lower energies than free charge carriers. This means they are often stimulated by sub-band-gap energies which can lead to increased device efficiencies. Moreover, depending on the band from which exciton originates, different types of exciton can simultaneously exist in the same material.

The probability of exciton creation is understood to be inversely proportional to both the band-gap energy and the dielectric constant of a material. The presence of other electrons has an impact on the electrical permittivity of a substance via screening of the electric field. This screening effect causes the Coulombic attraction between the electron-hole pair to negated, which in turn lowers the binding energy of the exciton, allowing for easier disassociation. Perovskites used in SCs usually have large dielectric constants, leading many to accredit the high number of free charge carriers to the low binding energy of excitons.

Excitons tend to be categorised into two groups, depending on their binding energies and, in turn, their sizes. The first excitons were proposed by Yakov Frenkel, in 1931 [30]. Frenkel excitons occur in materials with small dielectric constants, and characterised by binding energies of around 0.1 to 1 eV, leading to exciton sizes around the size of a unit cell. The second kind of excitons were discovered by Gregory Wannier and Nevill Francis Mott, and are known as Wannier-Mott excitons [31]. These occur in semiconductors, such as perovskites, with large dielectric constants. Due to their low binding energies of around 0.01 eV, they can have radii larger than the lattice spacing, leading them to also be known as large excitons. Their large radii are also favoured by the small effective masses found in semiconductors.

In 2015, Miyata et al. reported the first direct measurement of exciton binding energy and effective masses of the charge carriers [26] in $MAPbI_3$. Their experiment implemented high magnetic fields, of up to 65 T, in a temperature controlled environment. At temperatures as low as 2K, they identified the 1s, 2s and 2p excitons; clearly resolving the 1s exciton at 1.64 eV. They found excitons showed binding energies of 16 ± 2 meV and effective masses of $m^* = 0.104 \pm 0.003 m_e$, where m_e is electron rest mass. These results are close to those predicted theoretically by Mendez et al. [32] of $m^* = 0.099 m_e$. At room temperature, Miyata et al. reported exciton binding energies of only a few milli electron volts.

Furthermore, Zhang et al. found evidence supporting the low exciton binding energies in perovskites [27]. When seeking to study magnetic field effects in hybrid perovskite devices, they reported findings which suggested that the materials were not excitonic, like those found in SCs based on organic polymers. Rather that, magnetic field effects suggested that perovskites behave similarly to silicon SCs, with a high proportion of free carriers.

Thus, it would seem that the evidence found in the literature suggests charge carriers are mostly present in their free forms.

Free carrier properties have been shown to be exceptional in perovskites. Including high charge carrier mobility [33] and long diffusion lengths [34]. The latter being key to the ability to implement perovskites within thin film architectures.

2.1.2 Degradation

Although MAPI SCs have a well documented fabrication process and are relatively reproducible, they are known to rapidly degrade due to a variety of reasons. The degradation mechanisms are not yet fully understood, but are often broken down into two groups of factors: extrinsic and intrinsic.

Extrinsic factors include moisture, UV, oxygen, and temperature levels, all of which can cause both degradation independently or accelerate degradation when combined.

Intrinsic factors which cause, or catalyse, degradation include perovskite stoichiometry, ion migration and the strength of bonds between cations and anions.

The most commonly quoted degradation mechanism is that caused by moisture or humidity. This degradation pathway is known to be accelerated by elevated UV or temperature levels, and in some cases, electric fields [35]. In general, MAPI perovskites degrade beyond recognition within a matter of days or weeks, however there has been some progress, with reports of damp test survival for up to 1000 hours [36].

It has been suggested that water molecules have a tendency to form hydrogen bonds with cations in the perovskite lattice [37, 38]. Once water molecule densities reach a critical level within a certain region, a hydrated perovskite phase is said to exist. This reversible phase change, is thought to be the beginning of a non-reversible degradation described by the following reactions [39]

$$\mathrm{CH_3NH_3PbI_3} \xleftrightarrow{\mathrm{H_2O}} \mathrm{CH_3NH_3PbI}_{aqueous} + \mathrm{PbI_2} \tag{1}$$

$$\mathrm{CH_3NH_3PbI}_{aqueous} \leftrightarrow \mathrm{CH_3NH_2} + \mathrm{HI} \tag{2}$$

$$\mathrm{O_2} + 4\mathrm{HI} \leftrightarrow 2\mathrm{I_2} + 2\mathrm{H_2O} \tag{3}$$

Since this process itself releases water as a by-product, this means that it can become a run-away effect.

Other authors have suggested that the formation of ammonia and hydrogen iodide, catalysed by water, is the primary degradation pathway present in MAPI perovskites [40]. This reaction is described by [41]

$$\mathrm{CH_3NH_3PbI_3(s)} \xleftrightarrow{\mathrm{H_2O}} (-\mathrm{CH_2}-)(\mathrm{s}) + \mathrm{NH_3(g)} + \mathrm{HI(g)} + \mathrm{PbI_2(s)} \tag{4}$$

Among the other extrinsic factors, there is that of degradation via incident UV radiation. There is evidence to suggest that MAPI degrades with UV radiation

even when there is no oxygen or moisture present [42]. However degradation due to UV radiation is most notable when combined with other factors. Aside from the perovskite layer, TiO_2 is also known to degrade in the presence of UV radiation [43].

Temperature not only significantly influences the crystal structure, but has also been shown to lead to degradation of MAPI photo-active layer without the presence of oxygen or moisture [44]. In the case of temperature degradation, the same reaction as in (1) is thought to take place, but at a slower rate. This has also been shown to take place in $MAPbI_{3-X}Cl_X$ [45].

Increasing Stability Several ideas have been proposed in order to increase the lifespans of perovskite-based SCs, either by making devices more robust against extrinsic factors or by reducing intrinsic factors which contribute to degradation.

In terms of tackling the instabilities caused by humidity, researchers have identified several methods. These include better encapsulation [46] or the implementation of hydrophobic layers within devices [35]. There also exists the possibility of increasing the strength of inter-organic-halide bonds, making the reaction in (1) harder to take place.

Some authors have also noted that the Spiro-OMeTAD may not offer protection against extrinsic factors [38], suggesting that a move to inorganic hole transport layers, such as P3HT, would increase device lifetimes.

When it comes to UV-induced degradation, evidence has been found supporting the increased photostability of FA when compared to MA [47]. As highlighted previously, TiO_2 also decomposes in the presence of UV radiation. Better stability results have been obtained by doping it with Al or replacing it completely with SnO_2 [43]. However, these alternatives seem to lead to decreases in device efficiencies.

Another exciting avenue of research is that of two dimensional Ruddlesdden-Popper perovskites [48, 49]. Where perovskite layers of a few single sheets of crystals are used. These photo-active layers have lower efficiencies due to their increased band-gaps, but device efficiencies of up to 11.2% have been maintained over 10,000 hours [50].

In order to combat intrinsic factors, researchers have been led to substitute perovskite elements with ones found nearby in the periodic table. An example of this would be the substitution of iodine with bromine, chlorine or even fluorine. These days, compositional engineering of perovskite layers has emerged as common practice in order to harness the optoelectronic properties of the MAPI perovskite while making it more robust through partial or total substituting one of its cations or anions.

2.1.3 Compositional Engineering

Table 1 shows some of the most popular combinations of cations and anions used within perovskite SCs with the structure ABX_3 [51]. It should be noted that any combination of halides can be used for a given choice of cations.

Table 1: Commonly found organic-inorganic perovskite cations and anions

Large Cation [A]	Small Cation [B]	Anion [X]
Organic	Inorganic	Halide
MA (Methylammonium)	Pb	I
EA (Ethylammonium)	Sn	Br
DA (Diethylammonium)	Ge	Cl

Many authors have speculated whether the presence of the large organic cation can be correlated with the decrease in stability. Motivated by this, investigations have been made into the substitution of the organic MA cation with an inorganic one, such as cesium [48, 52]. Some of these results seem promising, with perovskites demonstrating increased levels of robustness against humidity and temperature.

There also exists the possibility of replacing MA with another large cation such as formamidinium (FA) [53], guanidinium (GA) [54], imidiazolium (IM) [55] or any other of those found in Table 1. Total replacement of the MA cation seems to reduce the stability of the films, however promising results have been found for partial replacement of small amounts, an example of this being GA, which seems to improve both morphology and stability [54]. It has also been shown that in cases where the MAPI perovskite is rendered useless within 20 days, mixed cation devices with $FA_{0.83}Cs_{0.17}Pb(I_{0.8}Br_{0.2})_3$ retain 70% of their PCE over the same time-scale [53].

Some also postulate that when included, IM seems to act as an effective passivator [55]. This is supported by PL tests with higher peak intensities, suggesting that non-radiative recombinations had been significantly reduced.

While many studies have focused on the inclusion of hybrid organic-inorganic lead halide based materials, tin has also been used [56, 57, 58]. These avenues of research have been stimulated by concerns that have been raised about the inclusion of lead, which is harmful to human-beings. Results for these tin-based perovskites have been under-whelming leading to many authors returning to their lead based competitors.

One of the unique properties of MA based perovskites which make them useful for a variety of applications is the tune-ability of their direct band-gap. A well studied manner of tuning the band-gap energy of perovskites is by altering halide

content to achieve the desired energies [59, 60, 52]. Perovskites based on these halides are of particular interest in the context of SC applications because they have gap energies which span the visible spectrum ($280 - 740$nm).

For these reasons, and due to the plentiful examples available in the literature and within the author's research group, this type of compositional engineering was selected as the topic for this Masters dissertation. It was decided to substitute the iodine halide in the well studied MAPI perovskite partially and totally with bromine and chlorine.

2.2 Methodology

2.2.1 Substrate Treatments

In this section the approach to the cleaning of the Fluorine-doped Tin Oxide (FTO) covered glass substrate will be compared, and contrasted, between three different sets of authors. We find that a common trait is that in all three cases at least one step involves cleaning the substrate with Hellmanex cleaning solution (diluted with water in a 2:98 vol/vol ratio), whether it be in an ultrasonic bath [16, 61] or scrubbing by hand with a brush [62], following the sample being rinsed with deionized water. Another common step is that of UV ozone treatment, although [62, 16] carry out the step for 15 minutes instead of the 30 minutes claimed in [61].

As for differences in methodology, [61] begins the cleaning process with 30 minutes of ultrasonification in an alkaline solution, whereas [16, 62] use two separate 15 minute ultrasonification steps involving isopropanol and acetone respectively. [16] even carries out an extra ultrasonification with ethanol. All three authors describe the importance of immediately drying the substrate after the ultrasonification process. Moreover [62] stresses that samples should not be let to dry between steps if undesired streaks are to be avoided and that samples be processed immediately after the cleaning process is complete.

Based upon the fact that all three methods give similarly high efficiencies, it would seem logical to assume that steps shared in common are more probable to have an impact on device performance, although clearly correlation does not imply causation. Based upon this, the author identifies the UV ozone treatment as the step with the highest impact on device performance. This is because although all three methodologies share the use of Hellmanex in common, this is always the first step, perhaps implying that it is most effective against larger impurities and "macroscopic dirtiness".

Based upon these postulations, the author carried out some rudimentary tests whereby some samples were cleaned with and without UV ozone or Hellmanex.

It was noted that when perovskite solution was placed on samples without UV ozone treatment, the solution did not spread out as easily, leading to non-uniform films during spin coating. Samples without Hellmanex treatment showed negligible differences. The results were based upon inspection by eye and are, by no means, a comprehensive or robust test.

Following the analysis presented in this section, the author decided to follow the safest procedure possible, within reason. Therefore all steps were carried out including the use of ethanol, which was only applied in one of the sources. The three ultra sound treatments were carried out for 15 minutes each, which is less than the half an hour reported in [61]. However the combined time of all the ultrasonification steps is on par with that reported by the source with the most time spent carrying out ultrasound treatment [16].

2.2.2 Deposition Techniques

Due to MAPI's large diffusion lengths [34] it can also be used within thin film architectures, meaning that many deposition techniques are available. Before selecting a methodology for the synthesis of perovskite films for photo-voltaic applications, it is important to be familiar with current methods, their advantages and disadvantages, and the results they tend to yield. This section will touch on several common techniques including: spin-coating, sequential deposition, vapour assisted deposition, thermal evaporation, ink jet printing, electro-chemical deposition and vacuum flash-assisted deposition.

Spin-coating seems to be the most popular deposition technique used within the laboratory, probably due to its ease of use and reliability of results. In simple terms, a solution is placed on top of a rotating substrate. The centrifugal force experienced by the solution causes it to spread out while the surface tension acts against this force. It is difficult to find a high quality perovskite SC in which spin-coating has not been used in at least one of the steps of its fabrication.

There are two types of spin coating: static and dynamic. Static spin-coating involves depositing the solution on top of the substrate before the spin programme is started, dynamic application involves spinning the substrate while the solution is applied.

Spin-coating is known to give highly uniform films with a controllable thickness. Downsides to spin-coating are the inability to scale up the process to commercial or industrial levels. These scalability problems stem from the inevitable wastage of solution which cannot be recycled without taking extra steps during preparation such as use of a tray. Large substrates also suffer from gradients in centrifugal forces across the substrate, eliminating the possibility of using spin-coating for samples much larger than a few centimetres squared. For more in-

formation on the theory behind how the rotation speed and conditions affect the spin coating result see [63].

Sequential deposition is a technique whereby one dips a solid, often Pb^{2+} powder, precursor film into a chemical bath solution. Within this bath, the large A cation and the X halide are found.

When synthesising $MAPbI_3$ this way, PbI_2 is infiltrated into TiO_2 nano-pores creating a thin coverage layer. This is then dipped into a MAI, dissolved in 2-propanol, causing the lead iodide to convert almost instantaneously into $MAPbI_3$. Authors report efficiencies as high as 17 % using this technique [64].

Mitzi et al [65] report using thermal evaporation to deposit $MAPbI_3$ for SC applications. In this set-up, the two precursors MAI and PbI_2 are placed in separate thermal evaporation boats before being simultaneously heated in a vacuum [66].

Leyden et al [67] and Chen et al [68] report using vapour assisted deposition with impressive results. They claim to be able to form both uniform and dense films. When implementing this technique, partial or total deposition of the perovskite layer is carried out by a carrier gas.

Vacuum flash-assisted deposition is sometimes implemented as a complementary step to the perovskite spin-coating process. After spin-coating takes place, the substrate is placed in a vacuum oven at 20 Pa for ten seconds, before being annealed at one hundred degrees centigrade under atmospheric pressure for half an hour. Following this, the spiro-OMeTAD layer is deposited as usual. The method has yielded high efficiencies of up to 20.5 % and smooth uniform films with large perovskite grains.

A relatively new fabrication method is that of ink jet printing (IJP), whereby the "jettable" solution often called an "ink" is ejected through a tiny nozzle (with a diameter around $20 - 100\mu m$). IJP was first used to make perovskite SCs in 2015, and has already achieved efficiencies of up to 13 %.

IJP has the advantage of being easily up-scalable using roll-to-roll techniques [69] and extremely precise with resolutions of up to 5000 drops-per-inch using drop-on demand techniques. Moreover, since the nozzle doesn't directly touch the surface of the sample, it can be applied to samples with exotic geometries. On the other hand, IJP like spin-coating, inevitable leads to wastage of the solution and very little research has been carried out on the "jettability" of commercially available "inks", let alone more unusual perovskite solutions that may be needing to be deposited.

In 2018, Han [70] reported the used of the doctor blade method to produce large perovskite modules with efficiencies of 14.6 % for an area of 57.2 cm^2. When this approach is adopted, the perovskite solution is applied to the substrate and then swiped by a glass blade at a fixed speed while held at an elevated temper-

ature. Doctor blade remains the most popular manner of producing large-scale perovskite samples, enabling high-speed deposition of uniform and large-area perovskite film, however large inhomogeneous islands and ring-like patterns are not uncommon.

Electro-chemical deposition has also been used in the synthesis of perovskite SCs. In 2018, Samu et al [71] reported successful deposition of the hole transport layer on top of a photo-active $MAPbI_3$ layer yielding devices with up to 5.9 % efficiencies. Electro-deposition techniques use polar molecules to deposit a given solution on top of an electrode. In the case of perovskites, this method has been held back by the instability of $MAPbI_3$ in polar solvents [72], however recent research has yielded promising results.

Since the objective of this Masters dissertation is to demonstrate the tune-ability of the perovskite layer and then to implement it within function devices at a purely research level, the scalability of the selected process was decided to be of lesser importance. Instead, the ease and accessibility of the methodology was deemed to be the priority. Reproducibility and consistence was also highly valued via studies of quantity and quality of the device efficiencies found in the literature. For these reasons, it was natural to select spin coating as the primary deposition technique.

Spin-coating was implemented for the study of the tune-ability of the band-gap in Section 3. During device fabrication, in Section 4, the majority of the layers including the perovskite, mesoporous and spiro-OMeTAD were also deposited via spin coating. The compact layer was deposited via spray-pyrolysis due to its ease of use and consistent results, which were verified by SEM. Clearly the gold contacts cannot be deposited via spin coating and were therefore applied via thermal evaporation.

3 Band-Gap and Compositional Engineering

This section is concerned with the band-gap tuning of methylamonium lead halide perovskites. The first section will present methodology, focusing on solution preparation and deposition. In the second part, samples will be characterised and results will be analysed.

3.1 Methodology

To demonstrate the tune-ability of the band-gap energy, five samples with $MAPbX_3$ and $MAPbX_{1.5}Y_{1.5}$ where X,Y= I, Br, Cl were selected. That is to say, one sample of each kind excluding $MAPbI_{1.5}Cl_{1.5}$. This is because chlorine has been shown to be able to act as a dopant, but attempts to increase the amount of chlorine above low concentration (around 3-4%) have been unsuccessful [73]. It is thought that this is could be due to the differences in atomic radii.

3.1.1 Solutions

To prepare the single-halide solutions, MAX and PbX_2 (where X=I, Br, Cl), were used as precursors. The MAI and PbX_2, (X=I, Br, Cl), precursors were purchased from Sigma Aldrich. The MACl and MABr precursors were synthesized in the laboratory.

To synthesize the MAX (X=Cl, Br), equimolar ratios of CH_3NH_2 (33% in ethanol, Sigma Aldrich) and HX (X=Cl, Br) (37% in water, Sigma Aldrich) were mixed together. Due to the exothermic nature of the acid-base reaction, HX (X=Br, Cl) was added drop-wise to a continuously stirred round-bottom flask, held in an ice bath, containing the MAH. This reaction is described by

$$HX_{aqueous} + CH_3NH_2 \rightarrow CH_3NH_3X + H_2O \tag{5}$$

Powders were then attained by using the rotary evaporator. Absolute ethanol was added to aide the crystallization before the powders were left to cool and filtered.

To synthesize the $MAPbI_3$ and $MAPbBr_3$ samples, equimolar PbX_2 and MAX (X=I, Br)(1.35M) were dissolved in a mixture of DMF and DMSO (1000:95 volumetric ratio); for $PbCl_2$ only DMSO was used.

Once the single-halide solutions have been prepared, the $MAPbI_{1.5}Br_{1.5}$ and $MAPbBr_{1.5}Cl_{1.5}$ solutions were prepared by mixing the corresponding single-halide solutions.

3.1.2 Glass Preparation

To begin, FTO covered glass (Pilkington TEC15) was thoroughly cleaned. Samples were placed step-wise in ultrasonic baths filled with a soapy solution (Hellmanex), ethanol (96% in water), acetone (99.6% in water) and 2-propanol (99.9% in water) for fifteen minutes. The samples were then dried with compressed air and placed in the UV ozone cleaner for a further fifteen minutes. The samples were then immediately inserted into an inert atmosphere for spin-coating.

3.1.3 Thin Film Deposition

For spin coating, samples were accelerated at 4000 RPM s^{-1}, before remaining at 4000 RPM for 50 seconds.

To begin, $50\,\mu l$ of perovskite is placed upon the substrate and allowed to spread out. Following this, an antisolvent-assisted single-step spin-coating process is employed. Whereby $150\,\mu l$ of chlorobenzene (CBn) is dynamically placed upon the substrate.

The purpose of this anti-solvent is to eliminate as much of the DMSO and DMF as possible, allowing the formation of a higher quality perovskite crystal structure. It should be noted that the dynamic application of the anti-solvent is one of the most critical steps in the process of the device preparation since there are many variables which contribute towards the formation of a high quality layer. These include the time in which the anti-solvent should be applied, which is dependent on humidity levels. The anti-solvent is also applied by hand so the precise time-wise application of the anti-solvent can be difficult. It is also possible to impart unwanted momentum on the anti-solvent as it is placed, leading to the non-negligible amounts of solvent pertaining in the samples.

The time between the initialisation of the spin programme and the application of the anti-solvent will be referred to as the application time. For $MAPbI_3$, $MAPbI_{1.5}Br_{1.5}$, $MAPbBr_3$ and $MAPbBr_{1.5}Cl_{1.5}$ samples, the application times were 6, 9, 4 and 20 seconds respectively. The $MAPbCl_3$ sample had no anti-solvent applied.

The application time is not well studied or documented in the literature, therefore a crude method had to be devised in order to determine this time. It should also be made clear that although CBn is known to work well with the MAPI perovskite, this is not the case for the remaining samples. In order to determine the application time, the first samples of each kind were spin coated without anti-solvent application in order to determine when a colour change took place. This colour change is thought to be due to perovskite crystallization and it is therefore necessary to apply any anti-solvent before then.

Of all the samples, deposition of the $MAPbCl_3$ was found to be the most difficult due to the extremely faint colour change which takes place during the spin-coating and the lack of information about deposition conditions within the literature. It is thought that the use of a colour sensitive sensor would allow the more precise detection of the temporal colour change. For these reasons, a systematic approach was taken where the anti-solvent was applied in ranges between five and fifteen seconds, with mixed results. In the end, the sample on which no anti-solvent was applied, was selected.

After each sample was spin coated, they were annealed at around 95°C.

3.1.4 Results

Following the aforementioned procedure, the best samples were selected. Figure 3 shows the samples chosen to be characterised.

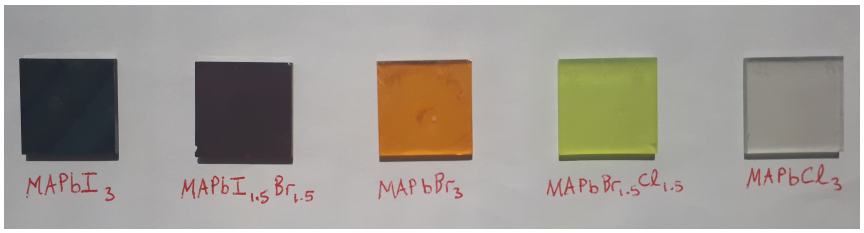

Figure 3: A photograph of samples with $MAPbX_3$ and $MAPbX_{1.5}Y_{1.5}$ where X,Y=I,Br,Cl.

3.2 Characterisation

In order to probe the quality of the crystalline structure and determine the gap energy, a combination of different techniques were used. These include photoluminescence (PL) tests, absorbancy tests and X-ray diffraction (XRD). The results are presented and discussed in this section.

3.2.1 XRD

The size of the octahedron, which is generically the crystalline structure of a perovskite, is known to be a function of the sizes of the anion, cation and halide respectively. Therefore substitution of the halides has a direct impact on the XRD spectrum since, although Cl, Br and I have the same number of valence electrons, they differ in the number of complete electronic shells. Thus it is expected that the peaks of the XRD spectrum will be shifted to larger angles as the size of the

halide, and therefore the inter-planar distance, is increased. This is exactly what is observed in Figure 4.

The observed behaviour of the shifting of the peaks can clearly be seen at the most intense diffraction peaks, located around $2\theta = 15^{\circ}$. This is the area of the graph that can be seen enlarged in Figure 5. The shifting of the peaks is also observed around the angles $2\theta = 30^{\circ}$. The reason that this shifting behaviour can be seen so clearly is because substitution of the halides does not change the cubic structure of the lattice, it only varies the lattice constant.

It can be seen that some peaks remain at constant angles throughout the samples, these are due to the FTO substrate and have been marked within Figure 4. These include the peaks at $2\theta = 26.47^{\circ}, 37.77^{\circ}$ which occur with a standard deviation of 0.06° and 0.03° respectively.

Other peaks that occur in the diffractogram are due to the unique presence of chlorine, bromine and iodine perovskites in each of the samples. Some peaks are also due to the presence of the halides by themselves, which are thought to have appeared due to degradation of the samples. The $MAPbI_3$ and $MAPbI_{1.5}Br_{1.5}$ samples can be seen to have non-zero diffraction intensities at values at which no peaks should occur, it is thought that this is due to the amorphous nature of the samples in question.

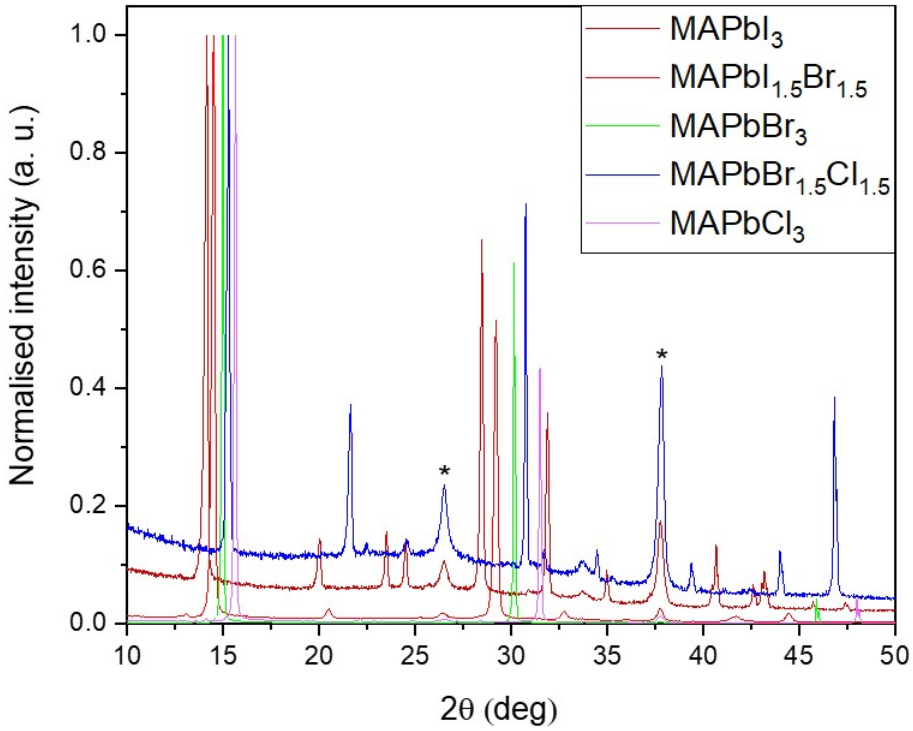

Figure 4: Shows the normalised spectra for samples with $MAPbX_3$ and $MAPbX_{1.5}Y_{1.5}$ where X,Y=I,Br,Cl. Stars mark the diffraction peaks due to the FTO substrate.

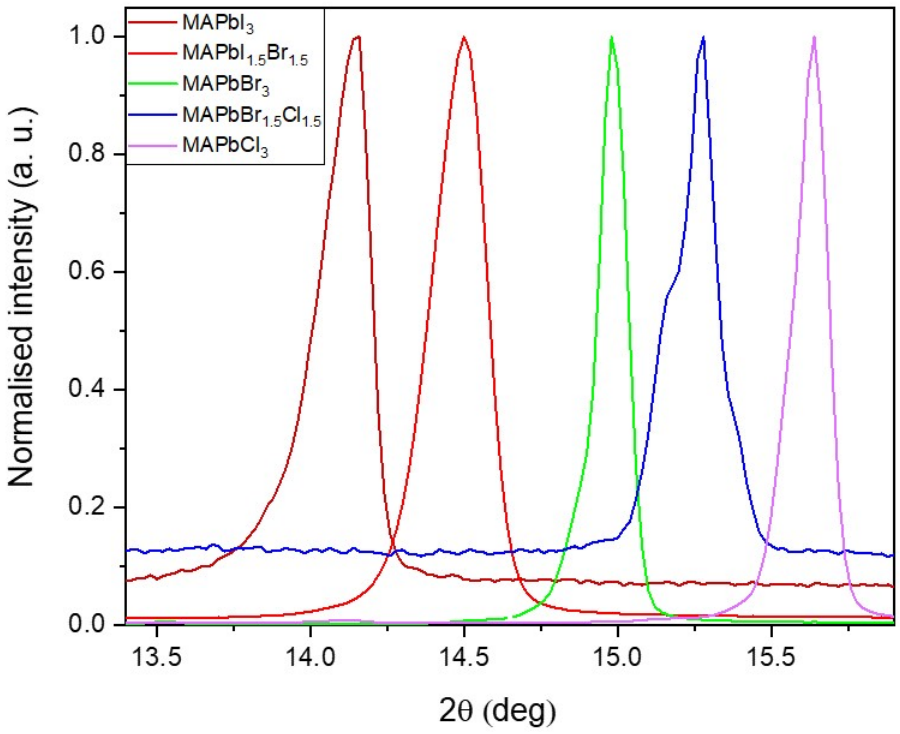

Figure 5: The spectra from Figure 4 centred on the most intense diffraction peaks.

From the width of the peak at half height (FWHM) it is possible to determine the sizes of the crystallites which make up the grains using Scherrer's approximation. Therefore if there are large variations in the widths of the peaks in a given XRD spectrum, then there is in turn a large variation in the sizes of the crystallites within the sample.

Table 2: Crystallite sizes calculated from dominant diffraction peaks

Sample	Crystallite size (Ang.)
$MAPbI_3$	440
$MAPbI_{1.5}Br_{1.5}$	405
$MAPbBr_3$	971
$MAPbBr_{1.5}Cl_{1.5}$	627
$MAPbCl_3$	645

Samples containing iodine had similar crystallite sizes, with an average size of just over 422 angstroms. Similarly, samples containing chlorine also had similar

sizes, with an average crystallite size of 636 angstroms. The major outlier within the data would be that of the $MAPbBr_3$ sample, with the dominant diffraction peak yielding a crystallite size of 971 angstroms. However peaks which yield sizes larger than 100 nm should be treated with caution, since Scherrer's equation is known to be unreliable in these regimes [74]. In the case of the pure bromine sample we have sizes close to this limit.

In the past it was thought that smaller crystallites and grains were better for the efficiencies of the perovskite absorbers however, nowadays, it is generally thought that the opposite is true. Large grain sizes reduce the amount of grain boundaries and pinholes within the layer, therefore having a beneficial effect on the efficiency of devices [75].

3.2.2 Transmittance and Absorbance

It can be insightful to measure the transmittance or absorbance of a sample of a given range of frequencies. In reality, it is only necessary to measure one of these since they are related straightforwardly by

$$A = Log(1/T) \tag{6}$$

where A is absorbance and T is transmittance of a sample at a given frequency. In this section, results for the said properties of the samples will be presented and analysed, determining the band-gap energy and the quality of the perovskite crystals. The former being more precisely calculated using a Tauc Plot, shown in Figure 8.

Transmittance Since photons incident on a given material can interact with only ions and electrons, photons with energies lower than those needed to promote these particles to more energetic quantum states are likely to pass through unimpeded. Moreover, since photons tend to interact mostly with electrons in a material, the quantity of those absorbed or transmitted gives us information about the energy separation between electronic quantum states in a material. That is to say, their band structure.

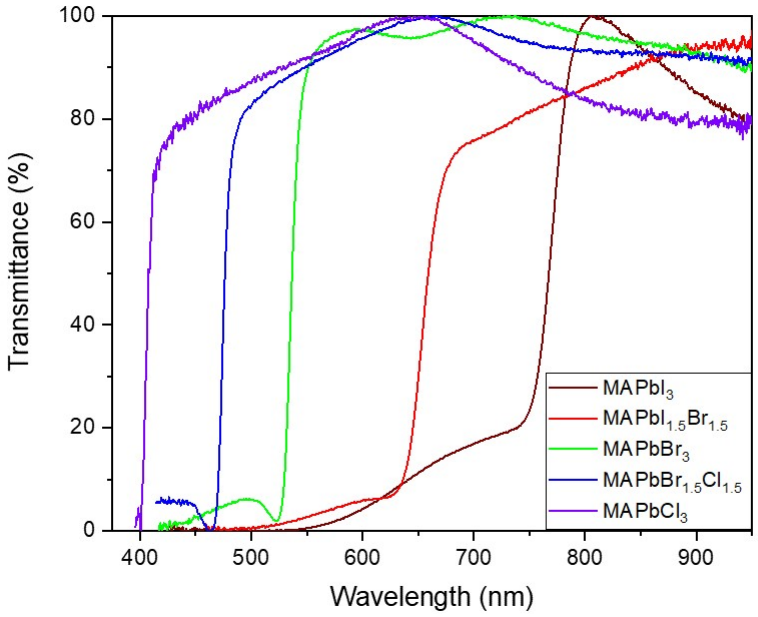

Figure 6: Shows absorbance as a function of incoming photon energy.

A brisk rise in transmittance at a given wavelength would therefore signal a significant decrease in the density of states with this energy difference. In most cases it is impossible to determine the nature of these transitions with the exception of semi-conductors, which by definition have "forbidden states" between the conduction and valence bands. In theory, unless a material is excited with the band-gap energy then electrons should be trapped in the valence band.

In reality, quantum effects (such as tunnelling), excitons and defects present in non-perfect crystals create states within the gap, causing sub-band-gap energies to be absorbed. This would lead to a non-vertical increase in transmittance, as a function of wavelength. The further the slope deviates from this ideal behaviour, the further the band-gap structure is also thought to deviate from "perfection". This is exactly the kind of behaviour that is observed in Figure 6.

Peak to peak and thickness Due to interference of light within the layer, it is possible to relate the distance between the highest peaks in the transmittance tests with the thickness of the sample. Identifying the transmittance maxima coupled with the assumption of a perfectly planar film allows the application of [76]

$$d_{thickness} = \frac{\lambda_1 \lambda_2}{2(n_1\lambda_1 - n_2\lambda_2)} \tag{7}$$

Where $d_{thickness}$ is the thickness of the layer, n_i is the refractive index and λ_i is the location of the transmittance maxima. Taking the values $\lambda_1 = 730$, $\lambda_2 = 592$ and $n_1 \approx n_2 \approx 1.75$[79] gives a film thickness of around 895 nm.

Since the other samples did not have multiple clearly defined maxima, it was not possible to apply (7).

Absorbance Similar to tranmisttance results, it is possible to estimate the gap of the perovskites prepared in Figure 7 by noting the energy at which the absorbance begins to occur.

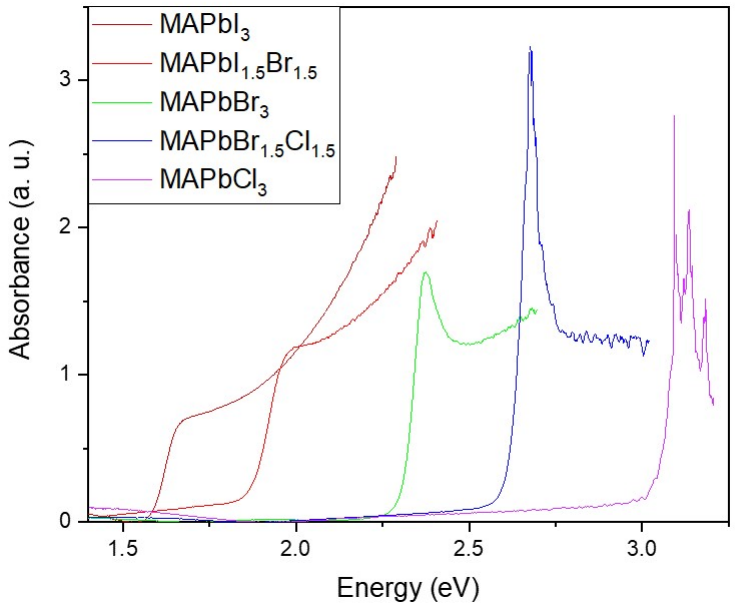

Figure 7: Shows absorbance as a function of incoming photon energy.

The curves shown in Figure 7 generically have a sudden increase in absorbance followed by a range of values in which the curve shows similar behaviour. We will refer to this range of values as the initial absorbance range (IAR). Following the IAR, behaviour of the curves changes dramatically; in the case of $MAPbCl_3$, $MAPbBr_{1.5}Cl_{1.5}$ and $MAPbBr_3$ the absorption peaks, before levelling off. For $MAPbI_3$ and $MAPbI_{1.5}Br_{1.5}$ the rate of increase in absorption becomes significantly lower after the IAR.

It is difficult to gain insights into the physical processes taking place within the samples after the IAR. This is because the dielectric function $\epsilon(\omega)$, which is a function of the angular frequency of the incident light, can be expressed in terms of reflectance and absorbance.

The slope of an IAR gives the Urbach energy, which gives information about the levels of disorder and crystalline structure in a given sample. In non-perfect crystals an exponential tail appears along the absorption curve near the optical band edge, due to localized states which lie inside the bandgap. This kind of behaviour is especially clear in the $MAPbI_{1.5}Br_{1.5}$ and $MAPbCl_3$ samples, but can also be seen in the $MAPbBr_{1.5}Cl_{1.5}$ sample to a lesser extent.

The slope of the IAR also gives us hints about whether the gap is indirect or direct. This is because excitations with a direct band-gap are more probable, therefore leading to a steeper slope. From simple observation of the curves in Figure 7 it is thought that all samples have a direct band-gap, however this can be confirmed using a Tauc plot.

Tauc Plot A Tauc Plot consist of plotting $(\alpha E)^x$, $x = 1/2, 2$, as a function of energy. In the case of a direct band-gap, choosing $x = 2$ will yield a linear curve. The latter will hold true in the case of an indirect band-gap for $x = 1/2$. Fitting a linear regression curve on a Tauc Plot and solving for the x intercept yields a value for the gap energy.

Table 3: Band-gap energy values calculated from the Tauc Plot.

Sample	Gap Energy (eV)	Wavelength (nm)
$MAPbI_3$	1.61	770
$MAPbI_{1.5}Br_{1.5}$	1.89	656
$MAPbBr_3$	2.31	537
$MAPbBr_{1.5}Cl_{1.5}$	2.61	475
$MAPbCl_3$	3.03	409

These energies can be seen to span the visible spectrum with mixed perovskites lying between their respective pure perovskite elements. The MAPI, $MAPbI_{1.5}Br_{1.5}$ and $MAPbBr_3$ samples show exceptional agreement with values found in [77], [78] and [79, 80], respectively. The remaining two samples are within 0.15 eV of values found in [81, 82].

3.2.3 Photoluminescence

During the PL test, a 405 nm purple laser was shone upon the samples. From straightforward observation by eye, samples containing bromine and chlorine

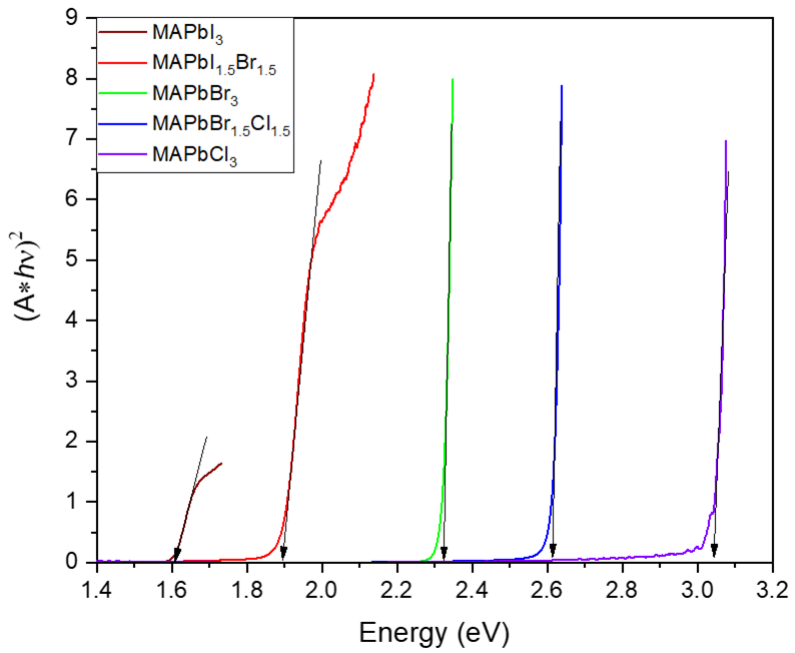

Figure 8: The Tauc Plot allows the better estimation of the gap energy by carrying out a linear fitting of the curve. This linear fitting is represented by an arrow.

were expectationally photo-luminescent, these are shown in Figures 9, 10 and 11.

Figure 9: Photograph taken of the inner chamber of the PL equipment with the bromine sample being illuminated.

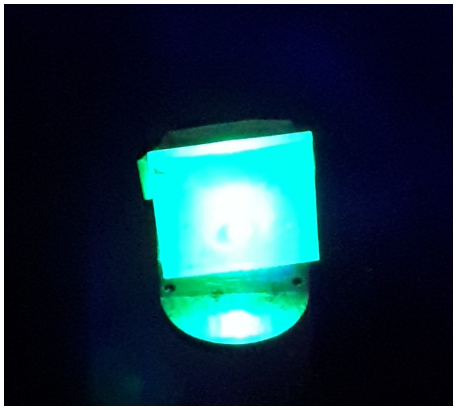

Figure 10: Photograph taken of the inner chamber of the PL equipment with the $MAPbBr_{1.5}Cl_{1.5}$ sample being illuminated.

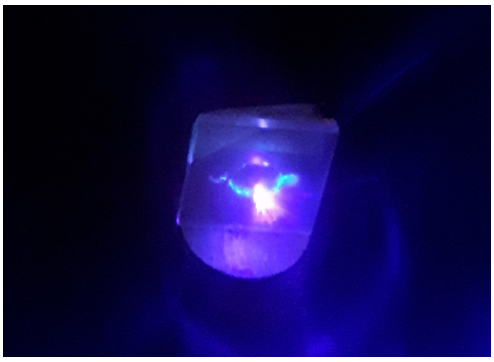

Figure 11: Photograph taken of the inner chamber of the PL equipment with the chlorine sample being illuminated.

Clearly this is a simple visual confirmation of the successful tune-ability of the band-gaps of these perovskite layers. Photo-luminescence of the samples changes from a strong green in the bromine sample to a softer purple in the chlorine sample, the mixture of the two having a colour that also lies somewhere between the two.

The photo-luminescence of the iodine samples was much weaker to the human eye, with the bromine-iodine mixture showing red spots as expected and the iodine sample having little-to-no photo-luminescence in the visible spectrum. It is thought that this is because the band-gap energy of the iodine sample falls within the infra-red part of the spectrum.

PL is a powerful tool for studying the band structure of semiconductors since any detected photons correspond to real electronic inter-band transitions. Only for perfect semiconductors, without defects or doping, will there be a narrow PL spectrum centred on the real gap energy E_g. This is because only band-band (B-B) transitions release photons with energy $h\nu \approx E_g$.

In reality, PL results will tend to give a maximum energy value which is *lower* than the real bandgap. This is because band-trap (B-T) and bound-band transitions always involve at least one electronic state within the bandgap. Moreover, donor-acceptor transitions can release photons of even lower energies since they involve two states within the band-gap. Since the measured PL spectra for a given crystal will be the sum of all the different types of transition, the width of PL peaks gives information about the probabilities and quantities of different electronic transitions between the conduction and the valence band.

Results Unfortunately due to technical issues, during the first set of PL measurements, the equipment used to measure the PL spectra was not calibrated properly and therefore results cannot be used to correctly translate between intensity location in terms of pixels into intensity in terms of wavelengths. This is why several weeks later a second set of measurements had to be made. The results were mixed, the pure samples were in excellent accordance with absorbance tests and the mixed samples showing poor behaviour associated with degradation. Since the filter used in front of the detector in both experimental sessions, needed to filter out the laser light, had a wavelength cut off point of 450 nm, it was not possible to detect the spectrum of the $MAPbCl_3$ sample. According to absorbance results (Table 2), it has a band-gap wavelength of 409 nm.

Although during the first set of experiments, precise determination of the band-gap energy was not possible for a given sample, the shape and behaviour of a given spectrum can still be studied even though it cannot be truly related to a wavelength. This includes the time-wise evolution of peak intensity, shown in Figures 12, 13, 14 and 15. Along the x-axis pixel number is shown, since calibration is needed to transform between pixel location and wavelength. In broad terms, a higher pixel number equates to lower wavelength.

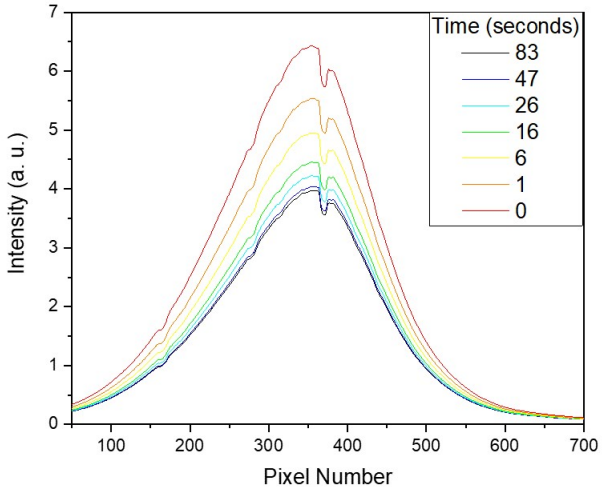

Figure 12: Time evolution in seconds for the PL spectrum of the $MAPbI_3$ sample. We see the intensity of the PL peak decrease with a lowering acceleration until an apparent equilibrium value is reached. During the evolution, the peak remains centred on the same value.

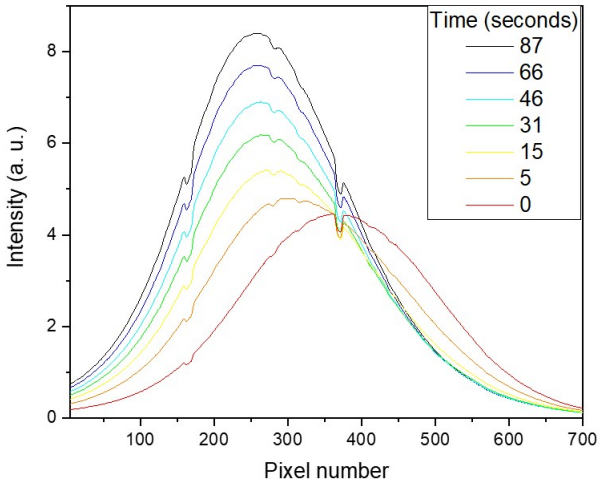

Figure 13: Time evolution in seconds for the PL spectrum of the $MAPbI_{1.5}Br_{1.5}$ sample. The intensity of the photo-luminescence can be seen to increase with the peak shifting to longer wavelengths.

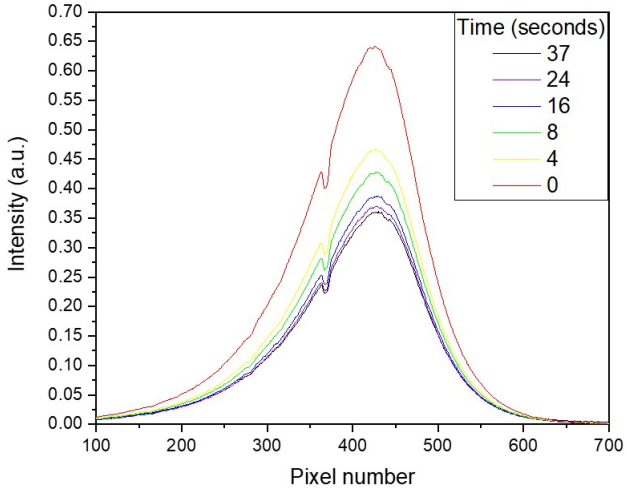

Figure 14: Time evolution in seconds for the PL spectrum of the $MAPbBr_3$ sample. We see the intensity of the PL peak decrease with a lowering acceleration until an apparent equilibrium value is reached. During the evolution, the peak remains centred on the same value.

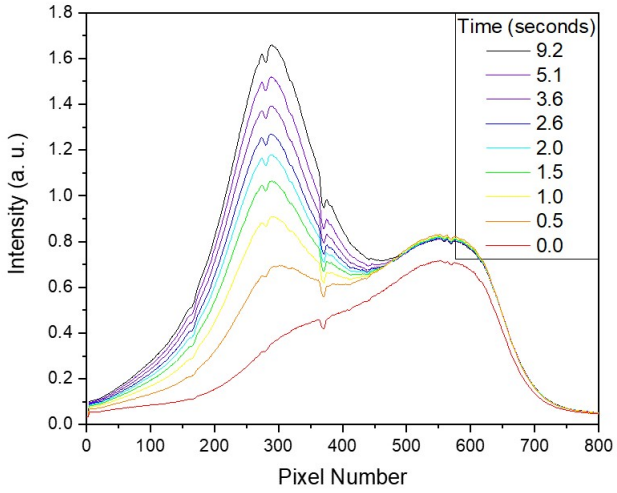

Figure 15: Time evolution in seconds for the PL spectrum of the $MAPbBr_{1.5}Cl_{1.5}$ sample. Although the original peak quickly reaches an equilibrium value, a new peak can be seen to arise at longer wavelengths.

For the pure samples, $MAPbI_3$ and $MAPbBr_3$, PL emission decreased over time. The remaining two mixtures showed surprising and unique behaviours with an increase in intensity and a shifting of the long-term peaks to longer wavelengths.

Observing the $MAPbBr_{1.5}Cl_{1.5}$ sample, the original peak can be seen to increase slightly, but for the most part, stays constant. However, after around one second, a new transition becomes the dominant peak in the PL spectrum. Moreover, the peak grows in intensity until reaching a value far larger than the original peak. This kind of behaviour suggests a more complex band structure or the existence of two different band-gaps due to impurities existing within the sample. It is possible that either not all the precursor elements were used up during the perovskite synthesis or that some precursor elements have arisen in the sample due to degradation. However without the precise determination of this peak's energy, it is impossible to verify the presence of other molecules.

It should be noted that all samples showed a dip in intensity around pixel number 380. It is believed that this is due to the incorrect set-up of the apparatus leading to interferences coming from the diffraction grating. Due to the quality of the PL data collected, all results should be interpreted with caution. The second set of results are more reliable but, since they were obtained several weeks later, the preliminary ones are presented as a degradation study.

The shifting of the PL peaks at this earlier stage already provides evidence of sample degradation. The existence of several components of the spectra potentially signals the presence of degradation products.

Below, in Figure 16, PL spectra for the second set of results are shown.

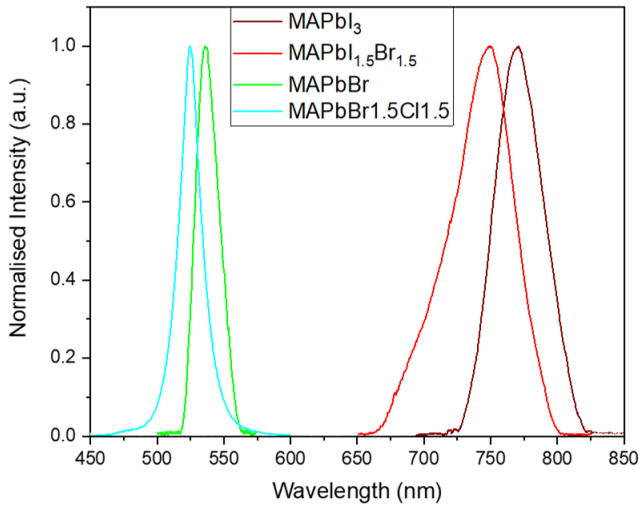

Figure 16: Spectra in terms of wavelength.

Surprisingly, PL spectra for samples containing iodine or bromine, are seen to group together and the more or less equidistant spacing between the band-gaps, shown in Figure 7, has been lost. It would appear that the MAPI and the MAPBr samples are located in the predicted energy ranges, however, the mixed samples have seen the PL spectra fall significantly in energy.

3.3 Results Analysis

MAPI results are in surprisingly good agreement with absorbance results given the time between the two measurements (see Figure 17). These results would seem to suggest the sample's robustness against degradation. Recall that in Section 2.1.2 we noted that some authors in the literature observed catastrophic degradation within a matter of weeks. The PL spectrum is made up of a Gaussian waveform, centered on 1.61 eV, which is the exact same result the Tauc Plot gave (Figure 8).

Placed within the context of the other spectra in Figure 16, we see that the MAPI perovskite does have a relatively wide spectrum, suggesting the existence of defects, excitons or other inter-band structures broadening the PL emission.

On the other hand, examination of Figure 16 reveals that the $MAPbI_{1.5}Br_{1.5}$ showed all the signs of degradation, namely the broad and asymmetric PL emission which overlaps with that of the MAPI perovskite.

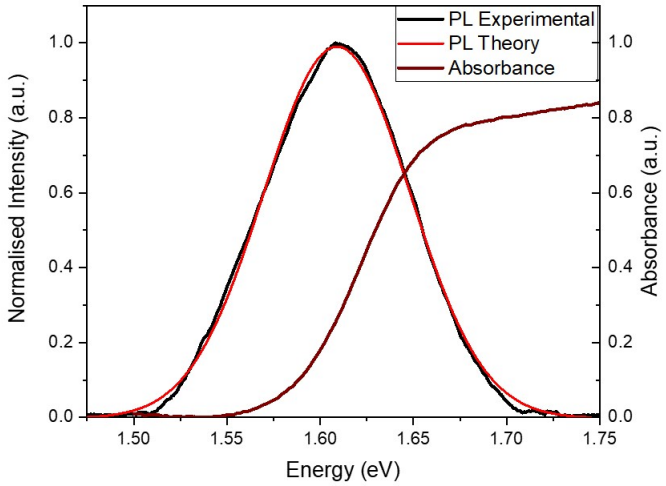

Figure 17: The PL spectrum for $MAPbI_3$ is super imposed upon the absorbency spectrum. The black curve denotes the data collected during PL tests and the red curve denotes the Gaussian which is predicted theoretically.

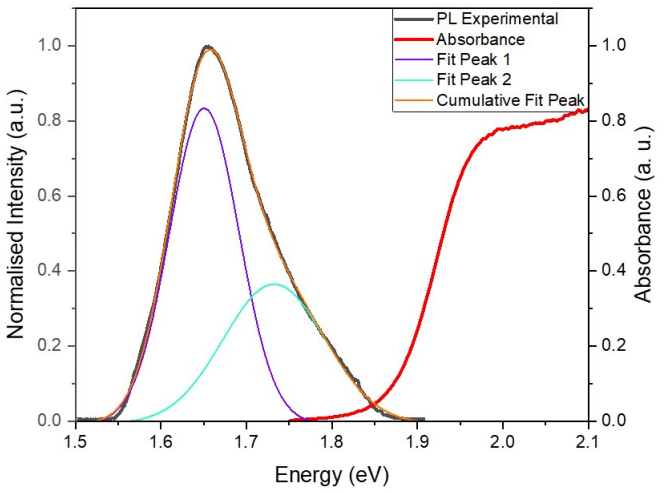

Figure 18: The PL spectrum for $MAPbI_{1.5}Br_{1.5}$ is super imposed upon the absorbency spectrum. The black curve denotes the data collected during PL tests and the brown curve denotes the Gaussian which is predicted theoretically.

Figure 18 shows the components of the PL spectra, where the dominant com-

ponent sits on the energy value centred over the MAPI band-gap energy. This is evidence for a significant amount of MAPI perovskite within the sample. Whether this quantity is residual or due to decomposition would require further investigation. Clearly even the higher energy component, of 1.73 eV, is still substantially below the absorbance results of 1.89 eV.

Focusing on Figure 16, results for the $MAPbBr_3$ are excellent, with a narrow peak centred on around 537nm which is in excellent agreement with absorption results (Table 2). In fact, we can see in Figure 19 that the spectrum is composed of two components. The dominant component has a maxima at a slightly higher energy of 2.32 eV, which is still in good agreement with absorbance. The secondary component of the spectra may comprise of defects or the presence of impurities.

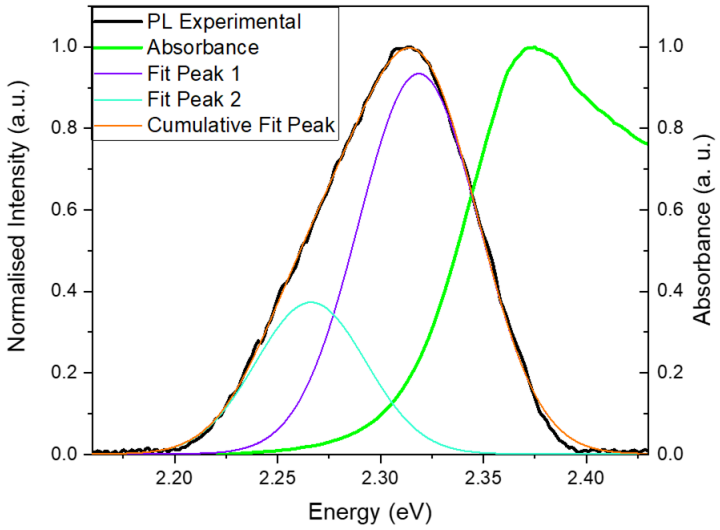

Figure 19: The PL spectrum for $MAPbBr_3$ is super imposed upon the absorbency spectrum. The black curve denotes the data collected during PL tests and the red curve denotes the Gaussian which is predicted theoretically.

To higher wavelengths in Figure 16 we have the $MAPbBr_{1.5}Cl_{1.5}$ sample. It is possible to see large overlaps of the $MAPbBr_{1.5}Cl_{1.5}$ spectra with that of the $MAPbBr_3$, potentially signalling decomposition. Although the spectrum is narrow, it is in poor agreement with absorbance results (see Figure 20).

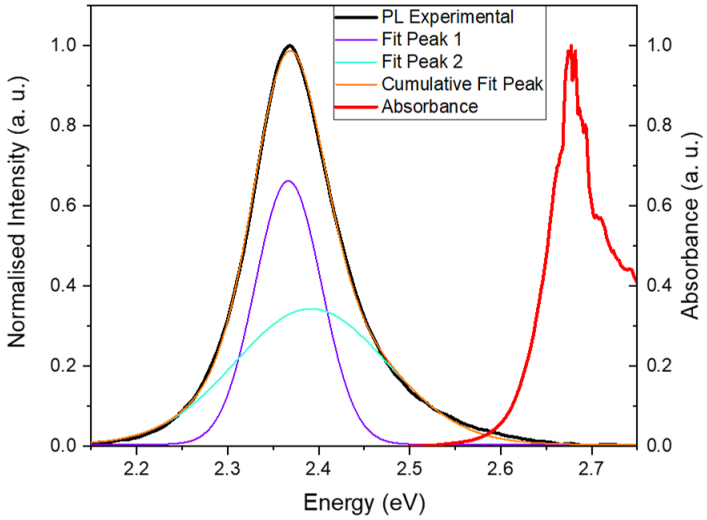

Figure 20: The PL spectrum for $MAPbBr_1.5Cl_1.5$ is super imposed upon the absorbency spectrum. The black curve denotes the data collected during PL tests and the orange curve denotes the Gaussian which is predicted theoretically.

Figure 20 suggests that the PL spectra is made up of two components, centred on 2.37 and 2.39 eV respectively. These are in poor agreement with absorbance results which yield a band-gap energy of 2.61 eV. These results seem to echo the first set of PL results, whereby we see in Figure 15 the appearance of a new peak at much lower energies.

Table 3: Band-gap energies values from absorbance and PL experiments. In the table, dominant component energy is given first.

Sample	Absorption (eV)	PL (eV)
$MAPbI_3$	1.61	1.61
$MAPbI_{1.5}Br_{1.5}$	1.89	1.65 & 1.73
$MAPbBr_3$	2.31	2.32 & 2.27
$MAPbBr_{1.5}Cl_{1.5}$	2.61	2.37 & 2.39
$MAPbCl_3$	3.03	—

3.4 Degradation study

Motivated by the poor PL results of the $MAPbI_{1.5}Br_{1.5}$ and $MAPbBr_{1.5}Cl_{1.5}$ samples, a study into XRD was made for completeness.

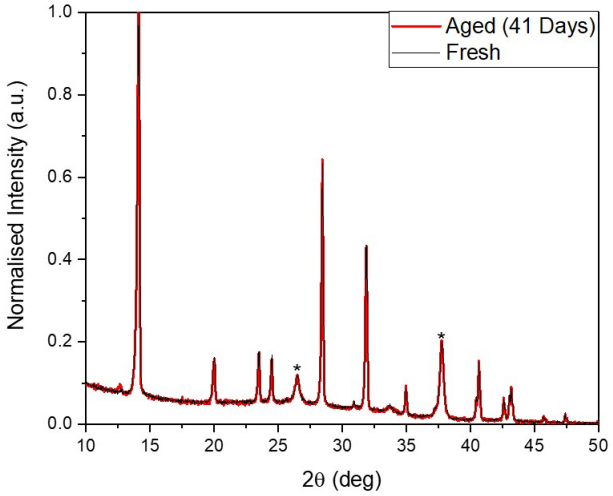

Figure 21: XRD results for the $MAPbI_3$ sample taken several weeks apart. Results are largely the same with the exception of a new peak which arises at 12.62°, which is due to the presence of PbI_2. Diffraction peaks for FTO substrate are marked with asterisks.

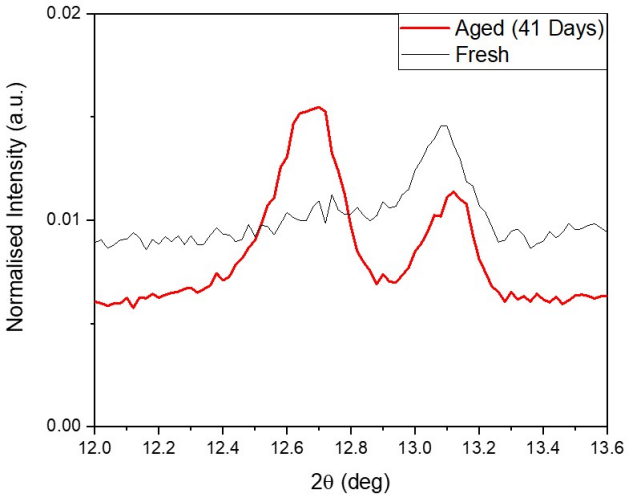

Figure 22: XRD results from Figure 21 centred on new diffraction peak at 12.62°.

Honing in on the ranges from 12° to 13.6° in Figure 21, we can clearly see the apparition of a new peak due to the presence of PbI_2. This is strong evidence for partial degradation of the sample, since it is a product of the degradation reaction described in (1).

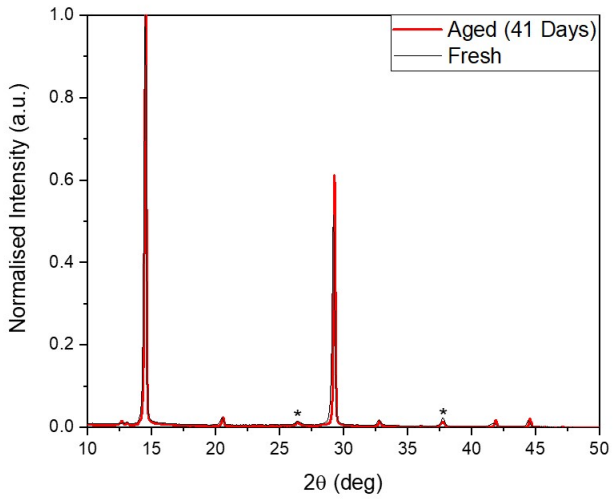

Figure 23: XRD results for the $MAPbI_{1.5}Br_{1.5}$ sample taken several weeks apart. Apart FTO substrate peaks (marked with asterisks), peaks can be seen to systematically shift to higher angles. A new peak, corresponding to the increased presence of PbI_2, is found at 12.64°.

As for the $MAPbI_{1.5}Br_{1.5}$ sample, we see the apparition of the PbI_2 peak at 12.6°. Peaks can also be seen to shift to higher angles, implying an increase in inter-planar distance. This global change in the crystalline structure suggests a poor robustness of the sample. Moreover this crystalline change could facilitate the creation of new defects in the lattice which could be the cause of the secondary component of the PL spectrum, found at 1.73 eV.

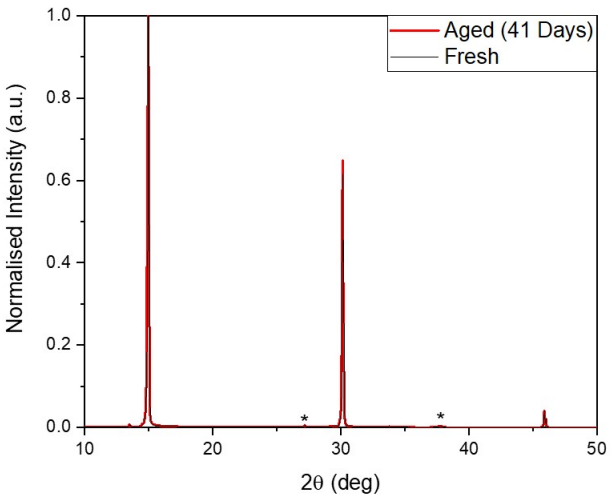

Figure 24: XRD results for the $MAPbBr_3$ sample taken several weeks apart. Results show the robustness of the sample, where little-to-no change has taken place in the crystalline structure. Diffraction peaks for FTO substrate are marked with asterisks.

The $MAPbBr_3$ sample showed impressive results, with no large scale changes in XRD behaviour. These results further highlight the sample as one of the candidates with the most desirable characteristics.

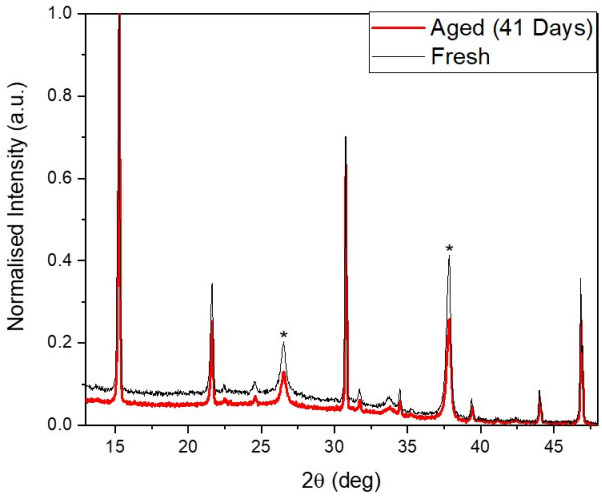

Figure 25: XRD results for the $MAPbBr_{1.5}Cl_{1.5}$ sample taken several weeks apart. Apart FTO substrate peaks (marked with asterisks), peaks can be seen to systematically shift to slightly higher angles. Moreover peak intensity is seen to decrease with respect to the dominant peak located at 15.28°.

As with the $MAPbI_{1.5}Br_{1.5}$ sample, the lattice constant seems to have increased as a function of time. These XRD results suggest the possible correlation between this crystalline behaviour and the large scale shifts seen in PL spectra (Figure 16). Relative peak intensities are also seen to decrease in the sample, suggesting an increase in disorder and the width of the distribution of inter-planar distances.

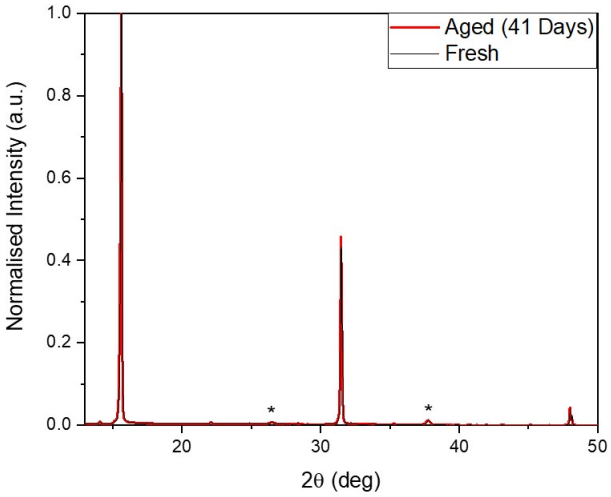

Figure 26: XRD results for the $MAPbCl_3$ sample taken several weeks apart. Results show the robustness of the sample, where little to now change has taken place in the crystalline structure. Diffraction peaks for FTO substrate are marked with asterisks.

Overall, the quality of the XRD results seem to coincide with the quality of the PL results. Shifts in inter-planar crystal distances are observed in both mixed samples, which also showed large shifts in their PL spectra. Moreover, the bromine sample showed near identical XRD spectra, correlating with the fact that the dominant PL peak coincided almost exactly with that of the absorbance test. Extrapolating the observed trends in the data, the $MAPbCl_3$ sample showed no noticeable changes in the XRD spectrum, suggesting that little-to-no degradation had taken place. Therefore it is expected that had its PL spectrum been measured, it would have been in excellent accordance with absorbance measurements.

4 Perovskite Solar Cells

Building upon the results yielded in the previous section, the perovskite layers are implemented in SC devices. Due to time constraints, a thorough analysis of device properties was not possible within this dissertation. Instead this section provides preliminary results to initiate further investigations, both experimentally and theoretically.

4.1 Methodology

Following the architecture described in Section 1.2.2, it was decided to opt for an conventional (n-i-p) set up with a mesoporous layer.

Substrate Preparation First of all, samples are partially etched. Tape is applied to the samples partially covering the conductive side, the rest is covered with zinc, shown in Figure 27. Application of hydrochloric acid (2M) then reacts with the zinc removing any conductive FTO. After all samples have been etched, samples are rinsed in water and a soapy solution (Hellmanex).

Figure 27: Applying Zinc for etching.

Glass substrates are then cleaned following the same process as in section 3.1.2. It is essential that the cleaning and preparation of the substrates is carried out in a clean and controlled environment since any problems will propagate

through the process impacting device efficiencies.

Compact layer To prepare the compact TiO_2 layer, 500 µl of titanium diisopropoxidebis (acetylacetonate) solution (75% in 2-propanol, Sigma Aldrich) is diluted in pure ethanol (1:9 volumetric ratio). This solution is applied via spray pyrolisis while the samples are held at 420°C in two rows of eight as shown in Figure 28.

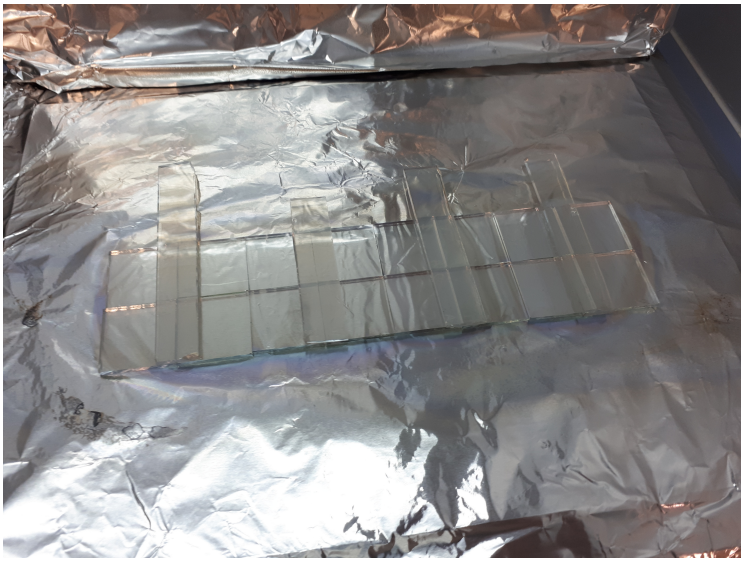

Figure 28: Set up for compact layer spray pyrolysis

.

Mesoporous Layer TiO_2 paste (Greatcell Solar 30-NR-D, 30nm average particle size) is diluted in pure ethanol (100:526 weight ratio). The vial is then placed on the roller and tilt mixer (Movil-rod) and agitated for twenty four hours.

The solution it is applied to the substrate via static spin-coating in an inert atmosphere. Before initiating the programme, 10 µl of the solution is placed onto, and allowed to cover, the substrate. Substrates are accelerated at 2000 $RPMs^{-1}$, after which they are held at this velocity for thirty seconds. Following the spin-coating programme, samples are placed directly onto a hotplate kept at 100 degrees. The set up is shown in Figure 29.

When all substrates have been coated they are placed on a heating ramp which reaches a maximum value of 500 °C. The samples are then left to cool to room

Figure 29: Set up for mesoporous layer spin-coating

.

temperature, before which they are removed. The preparation, deposition and annealing takes around six hours.

Perovkite Layer Following the same procedure as that in section 3.1.1, equimolar PbI_2 and MAI (1.35M) were dissolved in a mixture of DMF and DMSO (1000:95 volumetric ratio). 50 µl of perovskite solution was then applied via antisolvent-assisted single-step spin-coating, whereby samples were accelerated at 4000 RPM s^{-1}, before remaining at 4000 RPM for 50 seconds. 150 µl of chlorobenzene (CBn) was dynamically placed upon the substrate after 6 seconds of the programme being initiated.

Spiro-OMeTAD To prepare the hole-transport-layer, 72.3 mg of spiro (2,2',7,7'-tetrakis(N,N-di-p-methoxyphenylamine)-9,9-spirobifluorene) was dissolved in 1 ml of Cbn, 28.8µl of 4-tert-butylpyridine (TBP) and 17.5 µl of Lithium bis(trifluoromethylsufonyl)imide in acentorintle (520g/L).

50 µl of the aforementioned solution is then dynamically placed upon the substrate, after around 3 seconds, which is accelerated at 2000 $RPMs^{-1}$ before being held at 4000 RPM for half a minute. This should yield a shiny and brown coating.

Contacts After the spiro-OMeTAD has been left to oxidise, gold contacts are applied via evaporation (Leica EM MED020, shown in Figure 30).

Figure 30: Set up for evaporation of gold contacts.

4.2 Characterisation

During the first batch of devices it was noted that both the deposition of the mesoporous layer and the spiro-OMeTAD had radial lines and defects that could be seen with the naked eye. Based upon film quality, the decision was taken to not press ahead with the deposition of the gold contacts. Efficiency tests would have yielded poor results at the economic expense of the extra material used.

In order to achieve consistent layers, and high quality devices, a systematic approach was adopted studying each layer in turn.

4.2.1 Compact

In order to ascertain that film morphologies had the desired properties, an examination of three samples was made using SEM and transmittance tests. These three samples correspond to 2 edge samples and one middle sample in the set up shown in Figure 28. This was to ensure uniformity of the spray coverage over a range of samples, since the deposition is carried out by hand.

Scanning Electron Microscope As can be seen in Figure 31, films showed remarkable uniformity over large length scales. Moreover, few defects were found

and SEM results between samples showed striking similarity.

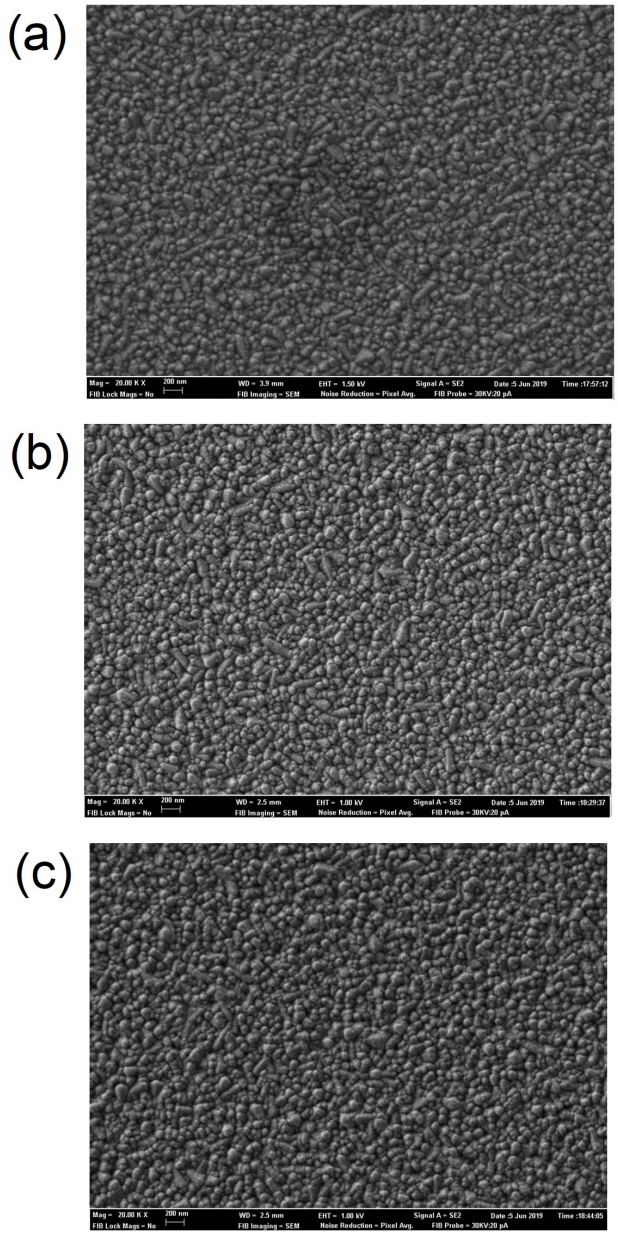

Figure 31: SEM image for samples corresponding to: (a) the far left, (b) the middle, (c) the far right hand side of the experimental set up shown in Figure 28.

Transmittance For transmittance tests, the middle sample was selected, although based on SEM results, all samples showed good morphologies.

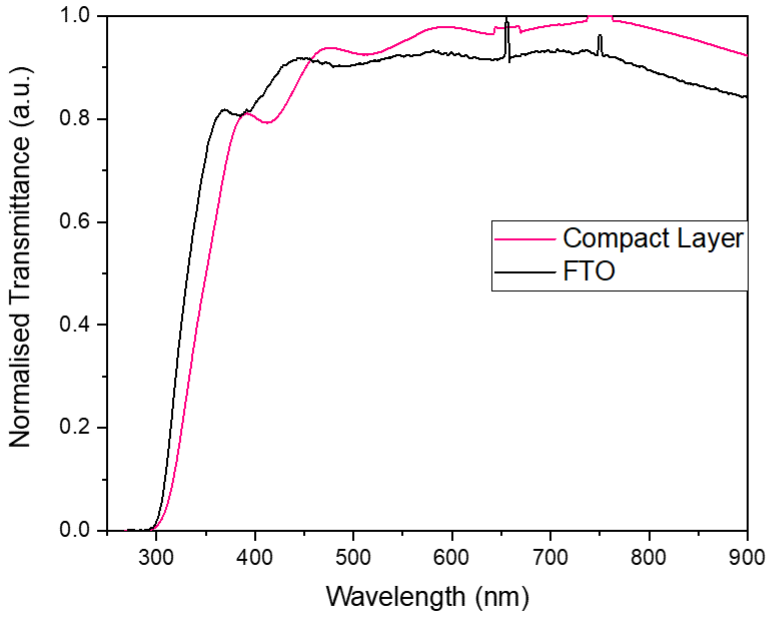

Figure 32: Normalised transmittance as a function of incident photon wavelength.

It can be seen that at lower wavelengths, transmittance decreases as the compact layer is added. However, at longer wavelengths, the transmittance actually increases! It is thought that this un-intuitive result can be understood in terms of the surface roughness of the sample.

If one considers light which is incident on the surface in a perpendicular manner, it is helpful to define light that has passed through the sample approximately parallel to the incident light as specular light. Often, however, light is reflected off the surface of the sample or diffracted through the sample leading to the outgoing photon having a large angle of deviation. These outgoing photons are denoted as diffuse light.

In the case in which the detector does not have the ability to detect the diffuse light, such as when a fibre optic cable is used, the detector will measure significantly lower transmittance than when a detector capable of detecting the diffuse

light, such as an interferometry sphere, is used. Thus the increased transmittance registered by the fibre optic cable when an extra layer is added, is in fact simply an increase in the quantity of specular light.

The increase in specular light can be understood by considering a ray incident on the new layer, which has a lower surface roughness. Due to the decreased roughness of the sample, there is of course a smaller quantity of diffuse light. Once inside the sample, when the ray reaches the boundary between the layers it finds itself being deviated small amounts since the difference in the refractive indices of the materials is smaller. Another way to say this is that given the same surface roughness, the amount of diffuse light is dependent on the refractive indexes of the materials at the boundary.

Implementing equation 7 and taking peak values $\lambda_1, \lambda_2 = 593, 477$ and $n_1, n_2 = 2.14, 2.21$ [83] yields a film thickness of 658 nm. This result is outside the widely accepted ideal value of around 50 nm [84]. This inconsistent result suggests the necessity to investigate the film thickness further using an another independent method, such as a cross-sectional SEM image, to determine the film thickness. Should it give similar values of film thickness, a change will have to be made in the spin-coating process, such as increasing spin-time or spin-velocity.

4.2.2 Mesoporous Layer

Due to the low film quality yielded in the first generation of devices, an investigation into spin-coating deposition conditions was deemed necessary. Although it is also possible that synthesized solutions could have contributed to the undesirable results found in the first generation devices, namely the quality or viscosity of the TiO_2 paste, there are far more controllable variables within the deposition of the film.

In the literature, various different speeds and timings are employed during the second stage of the spin coating process. Saliba et al [62] report using 4000 RPM for ten seconds however it is not uncommon to find examples of velocities as high as 5000 RPM [85]. Therefore in order to investigate the velocity with the best results, samples were spin coated from 2000 RPM up to 4000 RPM with steps of 500 RPM.

From simple observations made by eye, it seems that the ideal velocity lies somewhere between 3000 and 4000 RPM. Samples with lower RPMs continued to show a large number of radial lines. In order to further ascertain film quality, an investigation was made into the different mesoporous layers yielded using XRD, SEM and transmittance tests.

XRD First of all, an XRD examination is made in order to ascertain that the film has the correct composition.

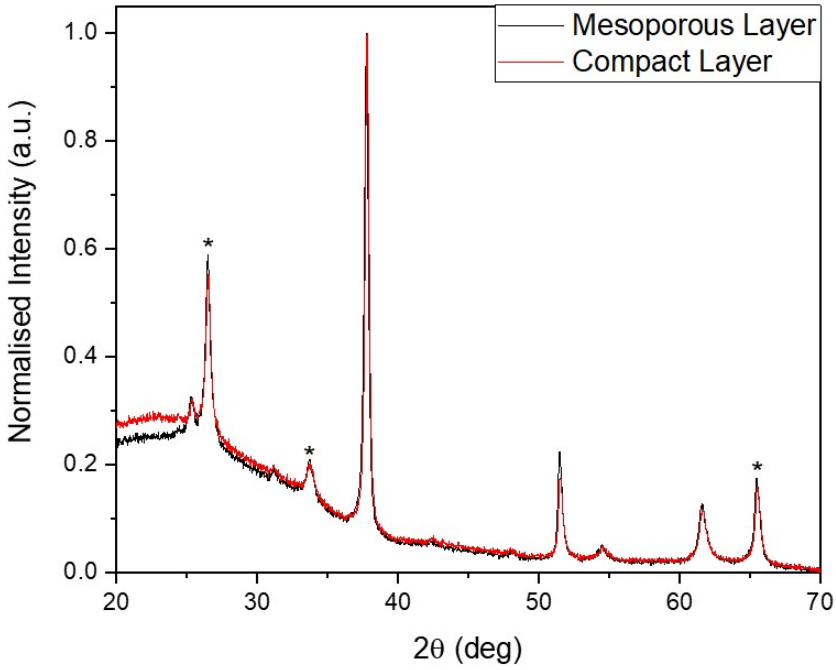

Figure 33: Normalised XRD intensity comparison between the compact layer and the mesoporous layer.

Since both layers comprise of TiO_2, XRD peaks are seen to arise at the same angles. Non-zero inter-peak values imply the existence of amorphous material. An increase in the amorphousness of the sample can be seen upon addition of the compact layer, however in general XRD data remains the same.

Scanning Electron Microscope Since the SEM can only accommodate for four samples, those coated at 2000, 2500, 3500 and 4000 RPM were selected. SEM results were very similar, with all films showing a uniform topology.

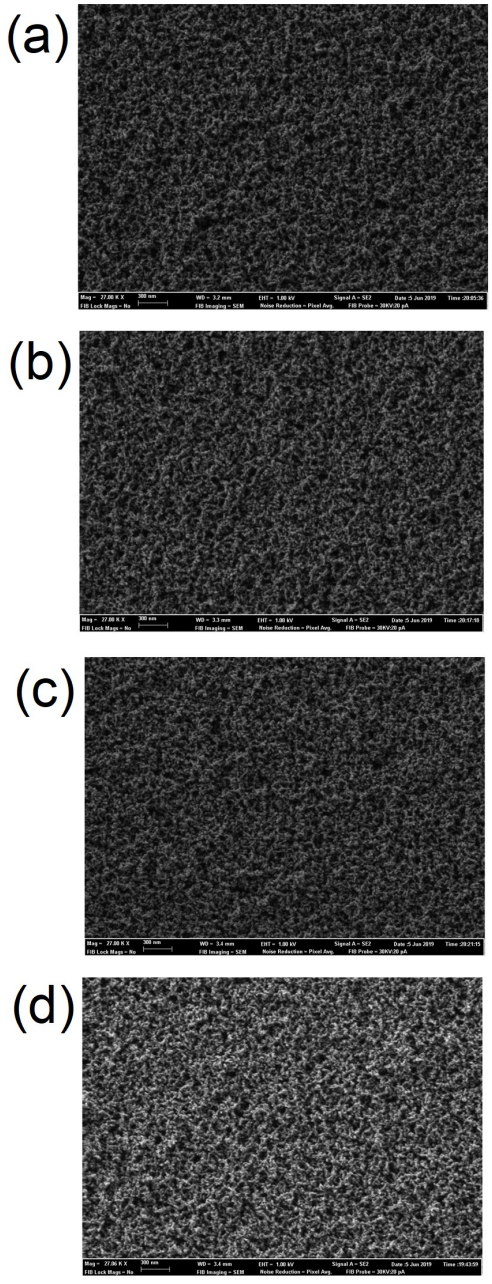

Figure 34: SEM images taken of the samples subject to the following velocities (RPM) during the second stage of spin-coating: (a) 2000, (b) 2500, (c) 3500 and (d) 4000.

Absorbance Figure 35 shows that the FTO substrate had the lowest absorption rate above 3.3 eV, with a tail that extended to lower energies. The addition of the compact layer simply added to the absorption of the substrate (see wavelength ranges between 300-480 nm is Figure 32).

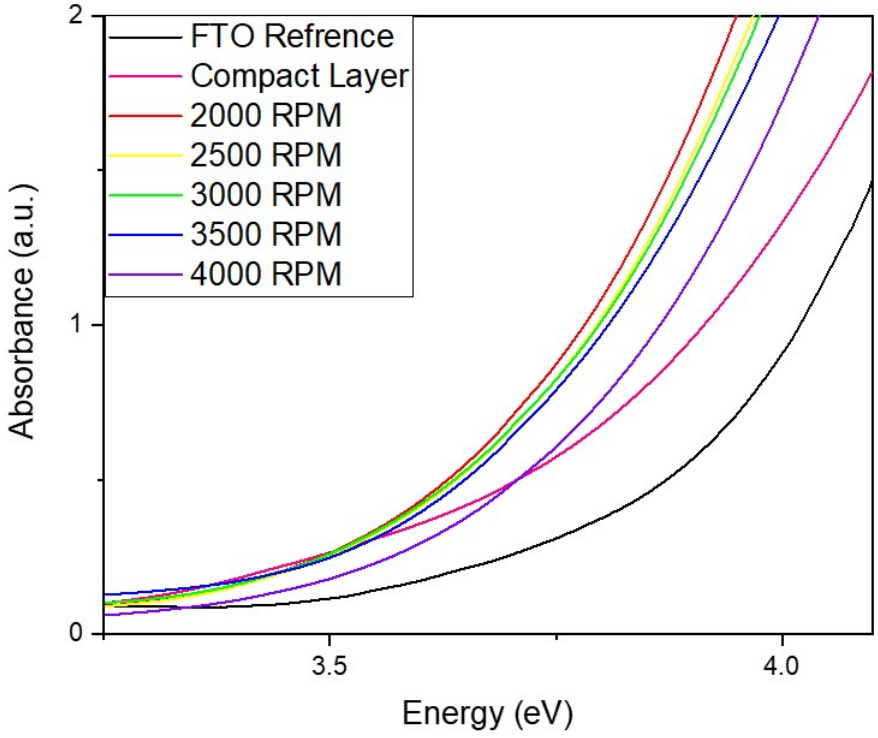

Figure 35: Absorbance, as a function of incident photon energy, for TiO_2 mesoporous layers deposited at angular velocities between 2000-4000 RPM. Absorbance results for the TiO_2 compact layer and the FTO covered glass substrate are also shown.

Interestingly, echoing results in the previous section, samples are seen to become more or less absorbent depending on the regime in question. Just below 3.5 eV we see a generic decrease in absorbance upon the addition of the mesoporous layer. On the other hand, by 3.75 eV, all samples with a mesoporpous layer showed increased absorbance.

Results for samples between 2000 and 3500 RPM are tightly localised. With a general shift to lower absorbance as RPM is increased. Potentially this could be due to the decreased thickness of the layers held at higher RPM. The sample held

at 4000 RPM shows a significant decrease in absorbance but retains the a similar behaviour in terms of curve shape.

Transmittance Assuming planar structures are yielded, transmittance tests allow for the estimation of the film thickness using equation 7. These are to be compared with the optimal thickness of the mesoporous film found in the literature.

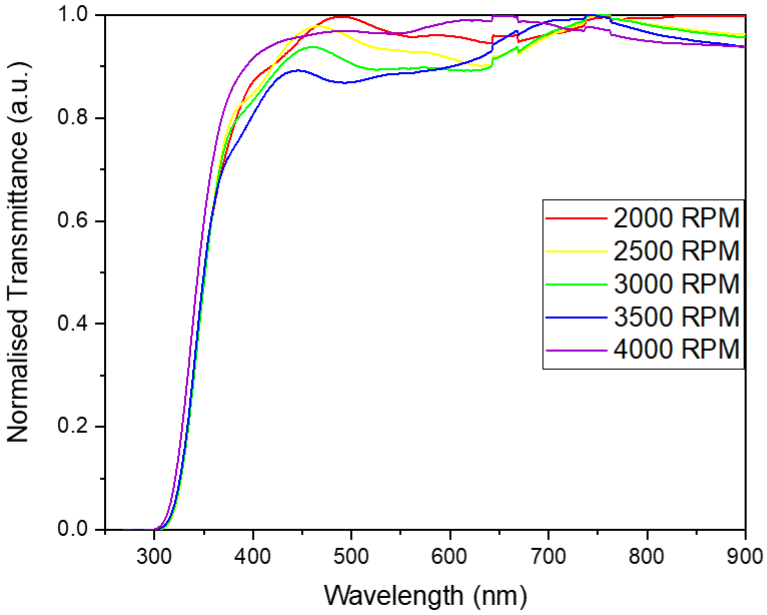

Figure 36: Normalised transmittance, of TiO_2 mesoporous layers, as a function of incident photon wavelength. Plateaux can be seen just above 650 and 750 nm, these are due to halogen lights used in the laboratory, not to an increased transmittance of the sample.

Table 4: Film thickness based upon transmittance maxima

Sample (RPM)	Maxima (λ_1, λ_2)	Refractive Index (n_1, n_2)	Thickness (nm)
2000	—, 492	—, 2.33	—
2500	757, 468	2.35, 2.52	295
3000	754, 460	2.35, 2.53	285
3500	737, 445	2.36, 2.56	276
4000	651, —	2.38, —	—

Refractive index values n_i are based upon those found in [83]. Roughly speaking, for the samples from 2500 to 3500 RPM, thickness is seen to reduce by 10 nm as RPM is increased by 500.

Deposition which took place at 2000 and 4000 only showed one clearly identifiable peak, with the 2000 RPM sample showing no others. The sample spun at 4000 RPM had a minor peak at 492 nm, but it is very poorly defined. Calculating film thickness using this minor peak yields a film thickness of 494 nm, which is clearly incorrect, since it suggests that film thickness increases with increasing angular velocity. It is thought that the lack of transmittance oscillation found in these samples is due to their non-uniform thicknesses, therefore impeding the application of equation 7, which holds only for planar films.

It is found that the film which was held at 3500 RPM, with a thickness of 276 nm, had the thickness closest to the 150-200 nm range which is typically claimed for high efficiency devices [62]. However it is slightly on the thicker-side, perhaps suggesting an increase in spin-coating time or RPM may benefit devices further .

4.2.3 MAPI Layer

To gain further insight into the relationship between macroscopic character of the sample and crystal quality, three samples of widely ranging perceived quality were selected for absorbance tests.

The best perovskite layer showed little-to-no cloudiness and with a brown-orange appearance. The average layer was relatively cloudy and had a centralised ring caused by the non-centered application of the anti-solvent. The worst sample was very cloudy and showed non uniform colours in a radial sense. It is thought that this range in color is due to the non-uniform thickness of the perovskite layer.

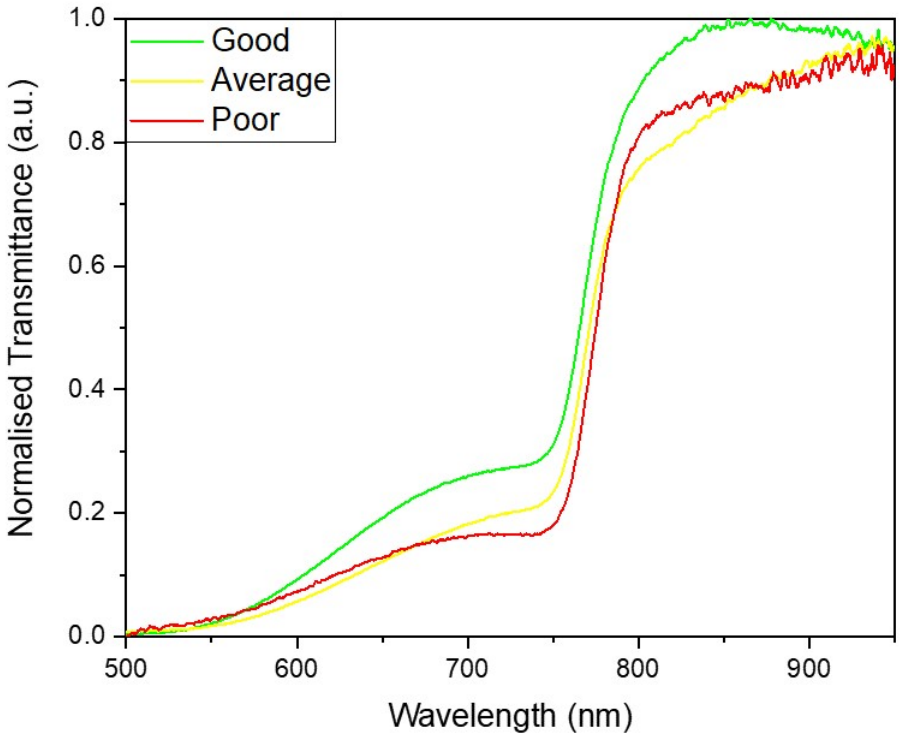

Figure 37: Normalised transmittance as a function of incident photon wavelength.

Figure 37 shows a startling similarity between the average and the poor sample. In fact the poor sample actually showed better overall behaviour, with a lower absorption below the band-gap, located at 770 nm (see Table 2). The poor sample also showed an increased absorption above the band-gap, highlighting the fact that macroscopic properties are not reliable indicators of perovskite layer quality.

The best MAPI layer showed the highest level of transmittance once the band-gap wavelength was reached. However, the sample also showed the highest amount of sub-band-gap transmittance, a property usually associated with a low defect density.

Comparing these results with those in Figure 6, all MAPI samples seem to show partial transmittance at wavelengths shorter than the band-gap. It is not known what the cause of this behaviour is and it is highlighted as an aspect which merits further study in the future. Especially since an increased transmittance of a sample has a knock on effect on device efficiency.

The good sample, as in Figure 6, also shows the apparition of what is thought to be excitonic transitions at around 850 nm.

Furthering the examination of the best MAPI layer, an assessment on film morphology was made using the SEM.

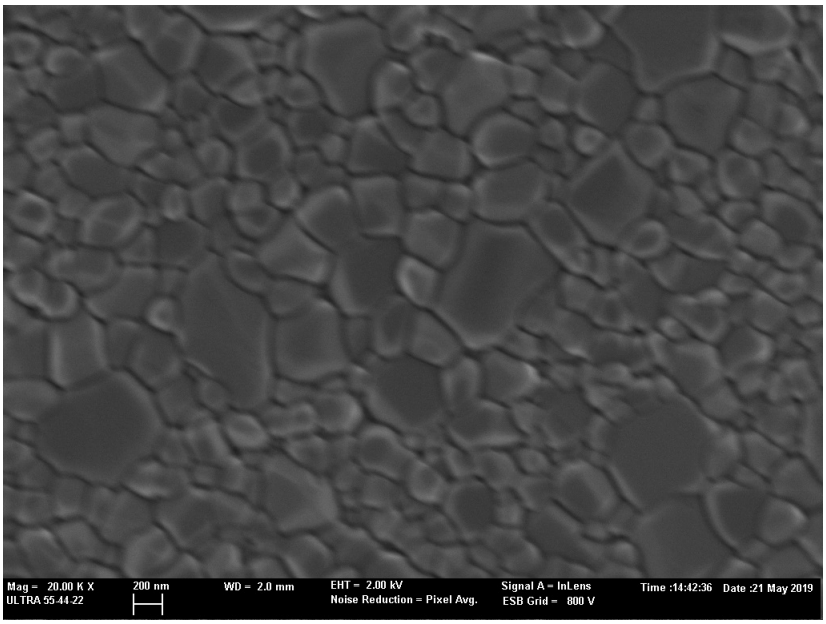

Figure 38: SEM image for the good MAPI sample shown in Figure 37.

SEM results for the MAPI sample demonstrated uniform film morphology over large regions, shown in Figure 38.

4.3 2nd Generation Devices

Following the second set of devices, all layers showed good characteristics by simple observation. This includes the mesoporous layer, whereby a new RPM of 3500 RPM was implemented in the second phase of spin coating.

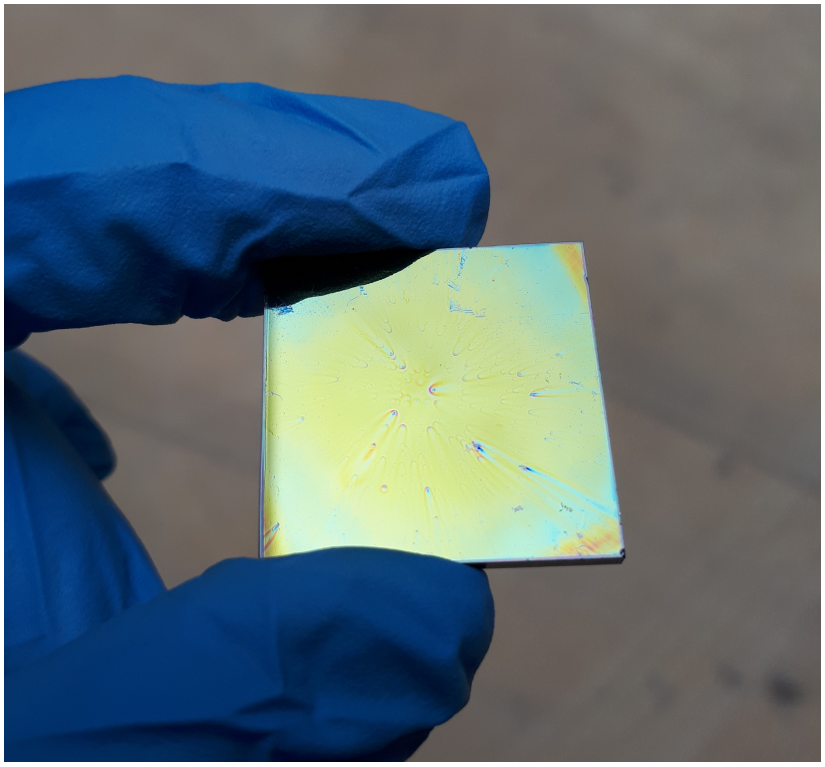

Figure 39: 2nd Generation of Devices

However, as can be see in Figure 39, the spiro-OMeTAD still showed poor properties. Colour changes take place in a radial sense, whereby a shiny-brown changes into a blue. It is thought that this is due to the non-uniformity of the film. Moreover, corners can be seen to be not covered properly, it could be that this is due to not allowing the solution enough time to spread out before the spin coating programme is started. Clearly, the sample still shows the radial lines present in the 1st generation of devices.

The findings about the overly large thickness of the compact film were also not taken into account during this second batch. Therefore several films need to be investigated further before the third generation of devices are made.

These preliminary results are an important step in the right direction. Having had the chance to practice synthesizing SCs and develop a methodology, the latter must now be refined in order to produce high quality devices.

5 Conclusions and Looking Forward

The study of hybrid organic-inorganic perovskites is motivated by the urgent need to accelerate a move to renewable energy sources. Perovskites have been identified as one of the fastest growing solar technologies with low barriers to entry.

In the first section, hybrid perovskites are introduced within the context of third generation solar panels, their working principles explained. Following this, the range of applications and properties that have been found in perovskites are presented. Some of these applications, such as LEDs and quantum dots, are highlighted since they share many similarities in terms of the physics taking place when compared to SCs.

The second section explores current research into perovskite SCs. The first part describing the properties of MAPI perovskites, including excitations and degradation. From this, the wider field of perovskite SCs is briefly examined in the context of compositional engineering via cationic or anionic substitution. The latter part of the literature review focuses on the methodology to be implemented within this research project, in particular, on substrate treatments and deposition techniques.

Armed with the aforementioned knowledge, the third and fourth sections cover the experimental part of this project. The third focusing on the tune-ability of the perovskite layer through compositional engineering and the fourth section implementing perovskite layers in SC devices.

5.1 Band-Gap Tune-ability

In the third section, the tune-ability of the perovskite absorber's band-gap was demonstrated, methodology is presented, from precursor synthesis to deposition conditions. The choice of selected samples is also discussed at the end of this section. Following the successful synthesis of the perovskite layers, they were characterised using XRD, absorbance and PL tests.

XRD results suggested the correct implementation of the procedure, whereby diffraction peaks are seen to shift (Figure 5) as a function of halide size. Crystallite size is also inferred from the FWHM of the diffraction peaks.

Absorbance tests gave promising results, summarised in Table 2. Band-gap energy was shown to be tuned depending on halide content and a direct band-gap was inferred from the Tauc Plot. The values yielded are in agreement with those found by other authors.

PL results were mixed, due to the time taken to access calibrated equipment. It is thought that the mixed samples containing iodine and bromine and bromine and chlorine, respectively, had already suffered from significant degradation by

the second set of PL results. In the first set of results, no data could be obtained about the energy values of PL emissions due to the un-calibrated set-up. However on the other hand, visual confirmation of the tunability of the band-gap can be seen in Figures 9, 10 and 11. The second set of results showed definite agreement with absorbance results for the pure samples, however large shifts were observed in the spectra of the mixed samples (see in Table 3).

Motivated by the need to explain the shift in PL spectra, an XRD analysis was conducted on the samples. As predicted, the $MAPbI_{1.5}Br_{1.5}$ sample showed the appearance of PbI_2, a clear signal of sample degradation. The $MAPbBr_{1.5}Cl_{1.5}$ sample also showed a significant decrease in diffraction peak intensities and a slight shift to higher angles. It is thought that these behaviours are also caused by sample degradation.

Clearly, some results produced during this project deviate from the ideal theoretical behaviour, such as the disagreement between band-gap energies calculated from the Tauc Plot and the PL tests. However, the author of this dissertation feels that further investigations carried out in order to explain these deviations provide satisfactory evidence for the existence of significant degradation in certain samples. Moreover, the degradation of photo-active perovskites is well documented in the literature. In fact, it is believed that these undesirable results can be wholly attributed to the approach adopted in the characterisation of the samples *rather than* the quality of the samples themselves.

Indeed, consider the fact that commonly in the literature researchers observe significant or sometimes catastrophic degradation within their MAPI samples within a month. Some of these examples are discussed in Section 2.1.2 on "Degradation". Consider then the startling results obtained within the second set of PL results, taken 50 days after sample synthesis, shown in Table 3. Not only does the PL spectra maximum coincide exactly with band-gap energy inferred from absorbance tests, taken 5 days after sample synthesis, but it is also in extremely precise agreement with the widely accepted value found in the literature. Although the second set of XRD data, taken 58 days after sample synthesis, does indicate degradation precesses taking place (Figure 22), the overall impression given by the collective results shows an extremely impressive robustness of the sample over a period of *two months*.

Furthermore, many of these points can be made of the $MAPbBr_3$ sample to an even larger extent. With the exception of the existence of a secondary component of the PL spectrum due to slight degradation (Figure 19), the bromine sample consistently outperformed the other samples, showing extraordinary luminescent properties (Figure 9) and wonderful agreement with documented results in the literature.

It is possible that the $MAPbCl_3$ sample would have also yielded strong results

based upon absorbance and XRD tests. However the restrictions imposed by the filter used in the PL set-up meant that without the added agreement from PL measurements, it was not possible to test this.

Whilst it is true that the mixed samples, containing more than one halide, did reveal slight shifts in band-gap energies at stages as early as the absorbance tests (taken 5 days after synthesis); the massively shifted band-gap energies found during the second set of PL results (Figure 16) correlate with the significant changes observed in their XRD spectra (Figures 23 and 25). Therefore, again, it is argued that the quality of the results presented within this dissertation are in fact closely related with the time-scales on which they were taken.

Based on the evidence presented it would seem reasonable to conclude that while sample quality is obviously critical, the structure of the characterisation of them is no less important. Only when samples have been characterised within a short period of time (ideally less than 24 hours) after synthesis, can properties and behaviours be truly analysed independently of degradation mechanisms, which physically change the character of the samples. That is unless the experiment or study is specifically concerned with these changes in behaviour *as* the sample degrades. In which case it follows that a different approach should be taken in order to study a different aspect of perovskite SCs.

Therefore, given that the purpose of this Masters dissertation was to develop a foundation for further investigations into the potential of perovskites as next-generation SCs, it would appear that the quality of the samples produced was of high enough to justify progressing to the next stage, implementing them in working devices.

5.2 Devices

In the fourth section, having gathered experience about the methodologies implemented within the previous section (on band-gap tune-ability), a recipe was formulated for the synthesis of MAPI SCs, with the help of the author's research group. This process, described in Section 4.1, along with the development of the necessary laboratory skills was lengthy and so the work presented here is simply a starting point.

Having carried out the process described in Section 4.1, it became apparent that film quality of several layers was clearly questionable on macroscopic length scales, prompting the need for a deeper and more systematic investigation into each layer in turn.

Starting with the compact layer, several samples on the edges and in the middle of the set up shown in Figure 28 were selected to ascertain whether the spray-pyrolysis, carried out by hand, was depositing uniform films with good

morphologies. SEM results were promising (Figure 31), where good morphologies were seen in all the samples with no distinguishable characteristics between them. Absorbance tests however, revealed that the samples had undesirable film thicknesses. In the literature, it is widely accepted that the optimum thickness for the film lies somewhere between 50-100nm. However, application of equation 7 gave a film thickness of over 650nm, which is off by an order of magnitude. Following this discovery, in the future it will be necessary to confirm this observation with independent experiments, such as a cross sectional SEM image. If this result is found to not be anomalous, it will be crucial to reduce this thickness in order to produce high efficiency devices.

Having identified macroscopic defects, such as radial lines, within the mesoporous layer after the first generation of devices, it was necessary to alter the process (Section 4.1). Since the synthesis of the solution to be deposited is fairly simple, and straight forward, it seems unlikely that this was the root of the problem. Especially since many authors in the literature, which have attained high quality devices, report using the same precursors. Moreover, discrepancies can be seen between the methodology in Section 4.1 and other authors in the literature (although it should be noted that many different methodologies are reported in the literature). It was therefore decided to study the spin-coating depositions, where RPM were varied in the second stage.

XRD and SEM results shed little light on which approach was most suitable, with no red flags found in either test (Figures 33 and 34). However, again, deviances were found between the film thickness as calculated with equation 7 and the optimum values found in the literature. Whilst not as large a difference as that found for the compact layer, the lowest thickness film of 276 nm was still above the ideal range of 150-200 nm. As with the compact layer, this result should be backed up with other experiments to confirm these findings with the possibility that RPM, or spin-time, should be increased further.

The final layer that was examined was the MAPI layer itself. As explained in Section 3.1.3, antisolvent-assisted single-step spin-coating is especially vulnerable to human induced error. The application of the anti-solvent, by hand, can quite literally make or break a device. For this reason, it was thought insightful to examine several MAPI layers in which the nature of the anti-solvent application varied significantly. Transmittance confirmed that the best-looking MAPI layer was indeed the one with the best properties. However, interestingly, the one that was identified from its macroscopic character to be the worst, actually performed better than the one that seemed average. These results would appear to suggest that while the highest quality layers do seem to be relatively identifiable from observation by eye, in practice, MAPI film quality and performance can only be truly deduced from further investigations. This poses an interesting problem since

during the manufacture of devices, often one wishes to save time and money by discarding samples that are deemed undesirable. However, these results highlight the dangers in doing so.

Having no oscillations in its transmittance spectrum, it was not possible to estimate the film thickness of the MAPI layer. Obviously, this aspect must be characterised if high quality devices are to be synthesized. On the other hand, SEM results suggest that films have good morphologies, meaning that no worrying results have been obtained in reference to this layer.

The second generation devices show that problems are still prevalent in the spiro-OMeTAD layer (Figure 39). This suggests the need not only to further refine the process, perhaps through the suggestions previously made, but also through the characterisation and tuning of the spiro-OMeTAD layer.

5.3 Looking Forward

These results provide a positive outlook for future work on the subject and the author has developed practical skills in the synthesis and characterisation of the preliminary devices, establishing a strong base upon which to build.

In terms of photovoltaic applications, the $MAPbI_3$ and $MAPbBr_3$ perovskites seem to be the most suitable due to their colour and following from the results presented within this dissertation. They both have a dark appearance (see Figure 3) in comparison to the other samples (especially the chlorine based one, which is semi-transparent), and would therefore absorb a higher amount of the solar spectrum. They are also some of the best studied perovskites, for solar applications.

Moreover, the $MAPbI_3$ and $MAPbBr_3$ samples showed some of the best stabilities when compared with the other samples, excluding $MAPbCl_3$. That said, many authors have noted the increased stability of MAPI perovskites when doped with chlorine, which leaves this open as a potential avenue for further investigation. The precision with which the MAPI and MAPBr samples band-gap values fell within the context of the literature was also outstanding. The $MAPbBr_3$ also showed impressive PL, where results clearly support its application in other devices such as LEDs. For these reasons, it seems logical to investigate these samples further.

In the future, new characterisation techniques could be used to determine the uniformity, thickness and behaviour of the samples. These might include the use of AFM, or an optical microscope, to map the surface of the sample. Temperature controlled experiments, such as PL, could also be implemented, since not only crystal phase changes, but also degradation pathways are known to be temperature dependent. Moreover, solar panels are subject to large temperature ranges when used in working environments and therefore understanding their proper-

ties within these working ranges is vital.

In the short term, it is hoped that research will focus on finalizing the work begun in section 4. Cross-sectional SEM images, ideally combined with other experiments, must be implemented to accurately, characterise film thicknesses, especially since these properties are known to impact device performance and have already been identified as a problem.

The study and mastering of the spiro-OMeTAD layer must also be completed to facilitate the synthesis of efficient devices. This would allow the deposition of the gold contacts and ultimately, tests of photovoltaic performance.

This should pave the way for developing the production process required to bring the human race one step closer to the ultra-efficient and low-cost renewable energy, that is desperately needed.

References

[1] M Cai et al., *Cost-Performance Analysis of Perovskite Solar Modules*, Advanced Science, Vol. 4, 1600269, https://doi.org/10.1002/advs.201600269 (2017)

[2] S. Kahmann & Maria A. Loi, *Hot carrier solar cells and the potential of perovskites for breaking the Shockley–Queisser limit*, Journal of Materials Chemistry C, 7, 2471-2486 (2019)

[3] H. J. Snaith, *Perovskites: the emergence of a new era for low-cost, high-efficiency solar cells*, J. Phys. Chem. Lett. 4, 3623–3630 (2013)

[4] F. Mathies, H. Eggers, B. Richards, G. Hernandez-Sosa, U. Lemmer & U. Paetzold, *Inkjet-Printed Triple Cation Perovskite Solar Cells*, ACS Applied Energy Materials, 1, 10, 1021/acsaem.8b00222 (2018)

[5] B. Dou et al, *Roll-to-Roll Printing of Perovskite Solar Cells*, ACS Energy Letters, Vol. 3, 2558-2565 (2018)

[6] M. Alsari et al., *Degradation Kinetics of Inverted Perovskite Solar Cells*, Scientific Reports, Volume 8, Article number: 5977 (2018)

[7] Research Cell Efficiency Records Charts., https://www.nrel.gov/pv/cell-efficiency.html [Last access: August 27, 2019], National Center for Photovoltaics (U.S. Department of Energy), 2019

[8] T. Rodziexicz, A. Zaremba & M. Waclawek, *Photovoltaics: Solar energy resources and the possibility of their use*, Ecological Chemistry and Engineering S. 23. 10.1515/eces-2016-0001 (2016)

[9] A. Lentz et al,, 2013 ISES Solar World Congress: Last Progress in CdTe/CdS Thin Film Solar Cell Fabrication Process, Energy Procedia, 57, 65-72 (2014).

[10] B. Mitzi et al., *Organic–inorganic perovskites: structural versatility for functional materials design*, IBM Hournal of Research and Development 45 (1), 29-45 (2001)

[11] Q. Zhao et al, *High efficiency perovskite quantum dot solar cells with charge separating heterostructure*, Nature Communications, Volume 10, Article number: 2842 (2019)

[12] K. Sharma, V. Sharma & S. S. Sharma, *Dye-Sensitized Solar Cells: Fundamentals and Current Status*, Nanoscale Res Lett., 13, 381, doi: 10.1186/s11671-018-2760-6 (2018)

[13] K. Liand et al., *Synthesis and Characterization of Organic-Inorganic Perovskite Thin Films Prepared Using a Versatile Two-Step Dipping Technique*, Chemistry of Materials, 10, 402- 411 (1998)

[14] J. Burschka et al, *Sequential deposition as a route to high-performance perovskite-sensitized solar cells*, Nature, 499, 316 - 319 (2013)

[15] G. E. Eperon, S. D. Stranks, C. Menelaou, M. B. Johnston, L. M. Herz & H. J. Snaith, *Formamidinium lead trihalide: a broadly tunable perovskite for efficient planar heterojunction solar cells*, Energy & Environmental Science, 7 (3): 982, doi:10.1039/C3EE43822H (2014)

[16] E. Vega, *Study and Characterization of Hybrid Organic-Inorganic Perovskites for Solar Cells Applications*, PhD Thesis, Universitat Politècnica de València (2019)

[17] M. Glazer, Bragg lecture 2017: The wondrous world of perovskites (Discourse), Friday 31 March

[18] J. Lloyd & J. Michinson, *What's the commonest material in the world?"*, QI: The Book of General Ignorance, Faber & Faber, ISBN 97820-0-571-233687 (2006)

[19] S.D. Stranks & H.J. Snaith, *Metal-halide perovskites for photovoltaic and light-emitting devices*, Nature Nanotechnology **10**(5):391-402 (2015), doi:10.1038/nnano.2015.90.ISSN 1748-3387.PMID 25947963

[20] M. Ban et al., *Solution-processed perovskite light emitting diodes with efficiency exceeding 15% through additive-controlled nanostructure tailoring*, Nature Communications, Vol. 9, 1-10 (2018)

[21] P.J. Dereń, A. Bednarkiewicz, Ph. Goldner & O. Guillot-Noël,*Laser action in* $LaAlO_3$: Nd^{3+} *single crystal*, Journal of Applied Physics, 103(4):043102-043102-8, doi:10.1063/1.2842399 (2008)

[22] E. J. Yoo et al., *Resistive Switching Behavior in Organic-Inorganic Hybrid CH3NH3PbI3-xClxPerovskite for Resistive Random Access Memory Devices*, Advanced Materials, Vol. 27, 6170-6175 (2015)

[23] J. M. D. Coey, M. Viret & S. von Molnar, *Mixed-valence manganites*, Advances in Physics 38(2): 167-293 (1999), doi: 10.1080/000187399243455

[24] L. Jingshan et al., *Water photolysis at 12.3% efficiency via perovsksite photovoltaics and Earth-abundant catalysts*, Science **345**(6204):1593-1596 (2014), doi:10.1126/science.1258307

[25] S. N. Habisreutinger, *Hysteresis Index: A Figure without Merit for Quantifying Hysteresis in Perovskite Solar Cells*, ACS Energy Letters, p2472-2476 (2018)

[26] Atsuhiko Miyata, Anatolie Mitioglu, Paulina Plochocka, Oliver Portugall, Jacob Tse-Wei Wang, Samuel D. Stranks, Henry J. Snaith, Robin J. Nicholas, *Direct Measurement of the Exciton Binding Energy and Effective Masses for Charge carriers in an Organic-Inorganic Tri-halide Perovskite*, Nature Physics volume 11, pages 582-587(2015)

[27] C. Zhang, D. Sun, C-X. Sheng, Y. X. Zhai, K. Mielczarek, A. Zakhidov & Z. V. Vardeny, Nature Physics volume 11, pages 427-434 (2015)

[28] V. D'Innocenzo, G. Grancini, M. J. P. Alcocer, A. R. S. Kandada, S. D. Stranks, M. M. Lee, G. Lanzani, H. J. Snaith et al., *Excitons versus free charges in organo-lead tri-halide perovskites*, Nature Communications. 5: 3586. Bibcode:2014NatCo...5E3586D.(2014), doi:10.1038/ncomms4586. PMID 24710005

[29] S. Collavini, S. F. Völker & J. L. Delgado, *Understanding the Outstanding Power Conversion Efficiency of Perovskite-Based Solar Cells*, Angewandte Chemie International Edition. 54 (34): 9757–9759 (2015), doi:10.1002/anie.201505321. PMID 26213261.

[30] J. Frenkel, *On the Transformation of light into Heat in Solids. I*, Physical Review, 37 (1): 17 (1931)

[31] G. Wannier & N. F. Mott , *The Structure of Electronic Excitation Levels in Insulating Crystals*, Physical Review, 52 (3): 191 (1937)

[32] E. Menendez-Proupin, P. Palacios, P. Wahnon & J.C. Conesa, *Self-consistent relativistic band structure of the CH3NH3PbI3 Perovskite*, Phys. Rev. B 90, 045207 (2014)

[33] L. M. Herz, *Charge-Carrier Mobilities in Metal Halide Perovskites: Fundamental Mechanisms and Limits*, ACS Energy Lett., 2, 7, 1539-1548 (2017)

[34] S. D. Stranks, G. E. Eperon, G. Grancini, C. Menelaou, M. J. P. Alcocer, T. Leijtens, L. M. Herz & A. Petrozza et al., *Electron-Hole Diffusion Lengths Exceeding 1 Micrometer in an Organometal Trihalide Perovskite Absorber*, Science. 342 (6156): 341–344. Bibcode:2013Sci...342..341S, doi:10.1126/science.1243982. PMID 24136964, (2013)

[35] A. Rajagopal, K. Yao & A. Jen, *Toward Perovskite Solar Cell Commercialization: A Perspective and Research Roadmap Based on Interfacial Engineering*, Advanced Materials, 30(32), 1800455 (2018)

[36] K. A. Bush et al., *23.6%-Efficient Monolithic Perovskite/Silicon Tandem Solar Cells With Improved Stability*, Nature Energy, Vol. 2, p1-7 (2017)

[37] G. Eperon, S. Habisreutinger, T. Leijtens, B. Bruijnaers, J. van Franeker, & D. deQuilettes et al, *The Importance of Moisture in Hybrid Lead Halide Perovskite Thin Film Fabrication*, ACS Nano, 9(9), 9380-9393 (2015)

[38] D. Wang, M. Wright, N. Elumalai, & A. Uddin, *Stability of perovskite solar cells*, Solar Energy Materials And Solar Cells, 147, 255-275 (2016)

[39] S. Emami, L. Andrade, & A. Mendes, *Recent Progress in Long-term Stability of Perovskite Solar Cells*, U. Porto Journal Of Engineering, 1(2), 52-62 (2018)

[40] J. C. Ke et al, *In situ investigation of degradation at organometal halide perovskite surfaces by X-ray photoelectron spectroscopy at realistic water vapour pressure*, Chemmical Communications, 53, 5231-5234 (2017)

[41] Y. Li, X. Xu, C. Wang, C. Wang, F. Xie, J. Yang & Y. Gao, J. Phys. Chem. C, 119, 23996 -24002 (2015)

[42] S. Lee, S. Kim, S. Bae, K. Cho, T. Chung & L. Mundt et al, *UV Degradation and Recovery of Perovskite Solar Cells*, Scientific Reports, 6(1) (2016)

[43] J. A. Christians et al., *Tailored interfaces of unencapsulated perovskite solar cells for >1,000 hour operational stability*, Nature Energy, Vol. 3, p68-74 (2018)

[44] B. Conings, J. Drijkoningen, N. Gauquelin, A. Babayigit, J. D'Haen, & L. D'Olieslaeger et al, *Intrinsic Thermal Instability of Methylammonium Lead Trihalide Perovskite*, Advanced Energy Materials, 5(15), 1500477 (2015)

[45] B. Philippe, B. Park, R. Lindblad, J. Oscarsson, S. Ahmadi, E. Johansson, & H. Rensmo, *Chemical and Electronic Structure Characterization of Lead Halide Perovskites and Stability Behavior under Different Exposures — A Photoelectron Spectroscopy Investigation*, Chemistry Of Materials, 27(5), 1720-1731 (2015)

[46] M. Wong-Stringer et al, *High-Performance Multilayer Encapsulation for Perovskite Photovoltaics*, Advanced Energy Materials, Vol. 8, p1-11 (2018)

[47] J. Lee, D. Kim, H. Kim, S. Seo, S. Cho & N. Park, *Formamidinium and Cesium Hybridization for Photo- and Moisture-Stable Perovskite Solar Cell*, Advanced Energy Materials, 5(20), 1501310 (2015)

[48] L. Iagher & L. Etgar, *Effect of Cs on the Stability and Photovoltaic Performance of 2D/3D Perovskite-Based Solar Cells*, ACS Energy Lett., 3, 2, 366-372 (2018)

[49] Z. Wang et al., *Efficient ambient-air-stable solar cells with 2D-3D heterostructured butylammonium-caesium-formamidinium lead halide perovskites*, Nature Energy, Vol. 2, p1-10 (2017).

[50] G. Grancini, C. Roldán-Carmona, I. Zimmermann, E. Mosconi, X. Lee, & D. Martineau et al, *One-Year stable perovskite solar cells by 2D/3D interface engineering*, Nature Communications, 8, 15684. doi: 10.1038/ncomms15684 (2017)

[51] B. M. Soucase, New materials for third generation photovoltaics. From concentration systems to low cost perovskites, 4th International Conference on Power Generation Systems and Renewable Energy Technologies (2018), Islamabad

[52] L. Atourki et al, *Impact of iodide substitution on the physical properties and stability of cesium lead halide perovskite thin films* $CsPbBr_{3-x}I_x$ ($0 \leq x \leq 1$), Journal of Alloys and Compounds, 702, 404 – 409 (2017)

[53] M. Alsari, A. J. Pearson, J. T. Wang, Z. Wang, A. Montisci, N. C. Greenham, H. J. Snaith, S. Lilliu & R. H. Friend, *Degradation Kinetics of Inverted Perovskite Solar Cells*, Scientific Reports, volume 8, Article number: 5977 (2018)

[54] X. Hou et al., *Effect of guanidinium on mesoscopic perovskite solar cells*, Journal of Materials Chemistry A, 5, 73 (2017)

[55] Q.. Wang et al., *Enhancing efficiency of perovskite solar cells by reducing defects through imidazolium cation incorporation*, Materials Today Energy, 7, 161-168 (2018)

[56] J. S. Manser, J. A. Christians & P. V. Kamat, *Intriguing Optoelectronic Properties of Metal Halide Perovskites*, Chem. Rev., 116 (21), pp 1295613008, DOI: 10.1021/acs.chemrev.6b00136 (2016)

[57] L. Hamers, Perovskites power up the solar industry (2017), Sciencenews. org. Accessed January 4, 2019.

[58] N. K. Noel, S. D. Stranks, A. Abate, C. Wehrenfennig, S. Guarnera, A. Haghighirad, A. Sadhanala, G. E. Eperon, S. K. Pathak, M. B. Johnston, A. Petrozza, L. M. Herz & H. J. Snaith , *Lead -free organici-inorganic tin halide perovskites for photovoltaic applications*, Energy & Environmental Science 7 (9): 3061, doi:10.1039/C4EE01076K (2014)

[59] L. Atourki et al, *Role of the chemical substitution on the structural and luminescence properties of the mixed halide perovskite thin $MAPbI_{3-x}Br_x$ ($0 \leq x \leq 1$) films*, Applied Surface Science, 371, 112–117 (2016)

[60] L. Atourki et al, *$MAPbI_{2.9-x}Br_xCl_{0.1}$ hybrid halide perovskites: Shedding light on the effect of chloride and bromide ions on structural and photoluminescence properties*, Applied Surface Science, 390, 744–750 (2016)

[61] N. Pellet, *Investigations on hybrid organic-inorganic perovskites for high performance solar cells*, PhD Thesis, ÉCOLE POLYTECHNIQUE FÉDÉRALE DE LAUSANNE (2017)

[62] M. Saliba et al., *How to Make over 20% Efficient Perovskite Solar Cells in Regular (n-i-p) and Inverted (p-i-n) Architectures*, Chemistry of Materials, 30, 4193-4201 (2018)

[63] *Spin Coating: A Guide to Theory and Techniques*, https://www.ossila.com/pages/spin-coating (Accessed: 01/07/2019)

[64] C. Momblona et al, *Research Update: Hybrid organic-inorganic perovskite (HOIP) thin fi*

lms and solar cells by vapor phase reaction, APL Materials, 2, 081504 (2014)

[65] A. Kojima et al, *Organometal Halide Perovskites as Visible-Light Sensitizers for Photovoltaic Cells*, J. AM. Chem. Soc. 131, 6050 (2009)

[66] S. Yang et al, *Iodide management in formamidinium-lead-halide-based perovskite layers for efficient solar cells*, Science, 356, 1376 (2017)

[67] C. Krebs et al, *25th Anniversary Article: Rise to Power OPV Based Solar Parks*, Adv. Mater, 26, 29 (2013)

[68] Q. Chen et al, *Planar Heterojunction Perovskite Solar Cells via Vapor-Assisted Solution Process*, Journal of the American Chemical society, 136, 622 - 625 (2014)

[69] D. M. K. Chondroudis, Chemistry of Materials, 11, 3028-3030 (1999)

[70] L. Han, *Surfactants for smoother films*, Nature Energy, Volume 3, pages 545–546 (2018)

[71] G. F. Samu, R. A. Scheidt, G. Zaiats, P. V. Kamat & C. Janáky, *Electrodeposition of Hole-Transport Layer on Methylammonium Lead Iodide Film: A Strategy To Assemble Perovskite Solar Cells*, Chem. Mater., 30, 13, 4202-4206, https://doi.org/10.1021/acs.chemmater.8b01521 (2018)

[72] K. L. Gardner, J. G. Tait, T. Merckx, W. Qiu, U. W. Paetzold, L. Kootstra, M. Jaysankar, R. Gehlhaar, D. Cheyns, P. Heremans & J. Poortmans, *Nonhazardous Solvent Systems for Processing Perovskite Photovoltaics*, Adv. Energy Mater. , 6, 1600386, DOI: 10.1002/aenm.201600386 (2016)

[73] S. Colella et al, *$MAPbI_{3-x}Cl_x$ Mixed Halide Perovskite for Hybrid Solar Cells: The Role of Chloride as Dopant on the Transport and Structural Properties*, Chemistry of Materials, 25, 4613-4618 (2013)

[74] N. Tamura & P. Gilbert, *X-Ray Microdiffraction of Biominerals*, Methods in enzymology, 532, 501-31. 10.1016/B978-0-12-416617-2.00021-7 (2013)

[75] B. Liu, S. Wang, Z. Ma, J. Ma, R. Ma & C. Wang, *High-performance perovskite solar cells with large grain-size obtained by the synergy of urea and dimethyl sulfoxide*, Applied Surface Science, Volumes 467–468, Pages 708-714 (2019)

[76] A. El-Denglawey, *Characterization of As–Se–Tl films near infrared region*, Journal of Non-Crystalline Solids, 357, 1757–1763 (2011)

[77] I. Levine, G. Hodes, H. J. Snaith & P. K. Nayak, *How to Avoid Artifacts in Surface Photovoltage Measurements: A Case Study with Halide Perovskites*, J. Phys. Chem. Lett. 8, 13, 2941-2943 (2017)

[78] L. Yuan et al, J. Mater. Chem. A, 6, 19696-19702 (2018)

[79] M. S. Alias et al, *Optical constants of CH3NH3PbBr3 perovskite thin films measured by spectroscopic ellipsometry*, Optics Express Vol. 24, Issue 15, pp. 16586-16594 (2016)

[80] Z. Gao, Y. Zheng, D. Zhao & J. Yu, *Spin-Coated CH3NH3PbBr3 Film Consisting of Micron-Scale Single Crystals Assisted with a Benzophenone Crystallizing Agent and Its Application in Perovskite Light-Emitting Diodes*, Nanomaterials, 8(10), 787, https://doi.org/10.3390/nano8100787 (2018)

[81] M. J. Islam et al, *Mixed-halide perovskite synthesis by chemical reaction and crystal nucleation under an optical potential*, NPG Asia Materials 11:31, https://doi.org/10.1038/s41427-019-0131 (2019)

[82] G. Maculan, *CH3NH3PbCl3 Single Crystals: Inverse Temperature Crystallization and Visible-Blind UV-Photodetector*, Phys. Chem. Lett. 6, 19, 3781-3786 (2015)

[83] Website: https://refractiveindex.info/?shelf=main&book=TiO2&page=Siefke, Accessed: 11/08/2019 13:04

[84] W. Qarony1, Y. A. Jui1, G. M. Das1, T. Mohsin1, M. I. Hossain1 & S. N. Islam1, *Optical Analysis in CH3NH3PbI3 and CH3NH3PbI2Cl Based Thin-Film Perovskite Solar Cell*, American Journal of Energy Research, Vol. 3, No. 2, pp 19-24. doi: 10.12691/ajer-3-2-1 (2015)

[85] V. Gonzalez-Pedro, E. J. Juarez-Perez, W. Arsyad, E. M. Barea, F. Fabregat-Santiago, I. Mora-Sero & J. Bisquert, *General Working Principles of CH3NH3PbX3 Perovskite Solar Cells*, Nano Lett.14, 2, 888-893 (2014)